Alpha Cluster Structure and Scattering in ^{20}Ne, ^{44}Ti, ^{94}Mo, ^{136}Te and ^{212}Po.

Joram Ndayishimye

Thesis presented in partial fulfilment
of the requirements for the degree of
Master of Science
at Stellenbosch University

Supervisor: Dr. Shaun M. Wyngaardt
Co-supervisor: Prof. Sandro. M. Perez
March, 2011

Declaration

By submitting this thesis electronically, I declare that the enterety of the work contained therein is my own, original work, that I am the sole author thereof (save to the extent explicitly otherwise stated), that reproduction and publication thereof by Stellenbosch University will not infrige any third party rights and that I have not previously in its enterety or in part submitted it for obtaining any qualification.

Joram Ndayishimye March, 2011

Abstract

We investigate the nuclei ^{20}Ne, ^{44}Ti, ^{94}Mo, ^{136}Te and ^{212}Po using a model of an α-cluster orbiting a closed shell core. A purely phenomenological cluster-core potential is found to provide a successful description of the spectra, B(E2$\downarrow$) transition strengths, and α-decay rates of the low-lying positive parity states of these nuclei. We then use the same potential as the real part of an optical model potential to describe the α elastic scattering by ^{16}O, ^{40}Ca, ^{90}Zr and ^{208}Pb. The experimental differential cross-section data are reasonably well reproduced with the imaginary potential depth as the only free parameter. The special case of the ^{8}Be system is also analysed.

Opsomming

Ons ondersoek die kerne ^{20}Ne, ^{44}Ti, ^{94}Mo, ^{136}Te en ^{212}Po deur gebruik te maak van 'n model waar 'n α-bondel om 'n kern met 'n geslote skil wentel. 'n Suiwer fenomenologiese bondel-kern potentiaal is gefind wat die energie spektra, B($E2\downarrow$) oorgangs sterktes, en α-verval tempo vir laagliggende positiewe pariteitstoestande vir hierdie kerne beskryf. Ons gebruik dieselfde potentiaal as the reële deel van die optiese potentiaal om die alpha elastiese verstrooiing deur die kerne ^{16}O, ^{40}Ca, ^{90}Zr en ^{208}Pb te beskryf. Die eksperimentele differentiele kansvlak data word redelike goed gereprodukseer met slegs die imaginêre potentiaal diepte as die enigste vrye parameter. Die spesiale geval van ^{8}Be is ook geondersoek.

Dedication

This work is dedicated to my brothers and sisters for their encouragement and prayers.

Acknowledgments

I am very thankful to the following people and institutions for the role they played in making this thesis possible:
Dr. S.M. Wyngaardt, supervisor, for his help, kind encouragement and helpful discussions.

Prof. S.M. Perez, co-supervisor, for suggesting the topic of research, and his guidance and suggestions.

Dr. T.T. Ibrahim, for many enthusiastic and indispensable discussions, his great support in my calculations.

Dr. J. Mabiala, for his assistance to get and use the standard code and the important software digitizer.

Dr. S.V. Förtsch, for his advice and orientation to the useful standard code.

All the members of the Physics Department, Stellenbosch University, for very stimulating and friendly atmosphere created by them.

The Stellenbosch University, the iThemba LABS and the African Institute for Mathematical Sciences (AIMS) for use of facilities and financial support.

I greatefully acknowledge the support of everyone in different ways, may God bless you all.

Contents

List of Tables

List of Figures

Chapter 1

Introduction:

1.1 Nuclear Models: An Overview

Due to the complex nature of the nucleon-nucleon interaction, and the relatively large number of nucleons in a typical nucleus, fundamental difficulties arise when attempting to treat a nucleus in terms of individual nucleons. It is then profitable to adopt an oversimplified theory, but one that is mathematically tractable and rich in physical insight. If that theory successfully accounts for at least a few nuclear properties, it can be extended and improved. Through such operations, a nuclear model is constructed.

Based on the unexpected α back scattering observed by Geiger and Marsden in 1911, Rutherford postulated his model of the nucleus in which the proton was considered as a fundamental particle [1]. Chadwick's discovery of the neutron in 1932 completed the basic picture of the nucleus that we have today, with the nucleons (protons and neutrons) as the basic constituents. More recently the internal structure of the nucleon has been probed revealing its three quark nature.

Various nuclear models have been proposed to describe the observed nuclear properties and of these the shell model, as well as the collective vibrational and rotational models described in the next section have played an important role. In this work we will examine a binary cluster model in which both the core and the α-cluster are doubly magic and apply it to ^{20}Ne, ^{44}Ti, ^{94}Mo, ^{136}Te and ^{212}Po, to predict spectra, decay properties and elastic α-scattering.

Although the data on ^{8}Be is less complete, with only the 0^+ ground state quasibound, we also extend our applications to this further example of a closed core plus α cluster system.

1.2 Shell Model

Nuclear Physicists have extended the use of the atomic theory based on the shell model to attack the problem of nuclear structure. In the atomic shell model, shells are filled with electrons in order of increasing energy, consistent with the requirements of the Pauli principle. In this model there is an inert core of filled shells and a remaining number of valence electrons, and it is assumed that the atomic properties are determined primarily by the valence electrons. Carrying this model over to the nuclear realm, some objections are encountered. The structure of the atom is governed by the rather weak and long range electromagnetic force while the nuclear force is strong and short range. Thus the electrons can move in orbits relatively free of collisions with other electrons whereas nucleons have a relatively short mean free path and interact strongly only with those nucleons nearest them. Thus the nuclear force saturates and the binding energy per nucleon and the central nucleon density are almost independent of the number of nucleons within the nucleus.
The independent particle model postulates that the nucleons move independently in an average potential and that the energy levels are filled from the lowest energy to the highest. Since all the low energy states are filled any residual scattering involves high energy final states and is thus reduced. So the nucleons can be said to move largely independently of one another, despite the strong short range nuclear force.
As is the case for the separation energies of electrons from some atoms a sudden and discontinuous behaviour in nuclear properties occurs at certain proton or neutron numbers. These so-called "magic numbers" (Z or N=2, 8, 20, 28, 50, 82, and 126) represent the effects of filled major shells, and any successful theory must be able to account for the existence of shell closures at those occupation numbers. Following from the inert nature of the closed-shell, the behaviour of nuclei either side of a shell closure is dominated by the extra or missing nucleons. When there is more than one valence nucleon the interaction between them is no longer negligible as, outside the closed shell, there are unoccupied low energy states. Then, an appropriate superposition of all the independent particle states is required to describe the system. The resulting shell model wavefunction for a many

valence nucleon system is complex and difficult to interpret [2].
The first step of developing the shell model is to choose an average potential such that the magic numbers are reproduced correctly. A simple choice like the square well for which

$$V_o(\vec{r}) = \begin{cases} -V_o, & r \leqslant R \\ 0, & r > R \end{cases} \tag{1.1}$$

where V_o of the order of MeV and $R \approx r_o A^{\frac{1}{3}}$ fm, with A the mass number and $r_o \approx 1.2$ fm the nuclear radius parameter, fails to reproduce the magic numbers, as does the harmonic oscillator defined by $V_o = \frac{1}{2} m\omega^2 r^2$. However by coupling the spin $\vec{s}$ of a nucleon to its orbital angular momentum $\vec{l}$ through a spin-orbit interaction, all the magic numbers can be reproduced. In this case, the Schrödinger equation becomes

$$\hat{H}\psi = \left[-\frac{\hbar^2}{2m}\nabla^2 + V_o(r) + V_{s.o}(r)\vec{l}.\vec{s} \right] \psi = E\psi \tag{1.2}$$

with each independent particle state an eigenfunction of $\hat{H}$. The spin-orbit interaction splits the $2(2l+1)$ degeneracy of each level into two levels of degeneracy $(2j_+ + 1)$ and $(2j_- + 1)$ where the total angular momentum is $\vec{j} = \vec{l} + \vec{s}$ and $j_\pm = l \pm \frac{1}{2}$.
A successful form of the independent particle nuclear potential is the Saxon Woods potential whose form mimics the nuclear density and reproduces the properties of closed shell ± 1 nucleon nuclei [3]. Its general form is

$$V(r) = V_c(r) - V_o f(r, R_n, a_n) - V_{s.o} \left(\frac{\hbar}{m_\pi c} \right)^2 \frac{1}{r} \frac{d}{dr} f(r, R_{s.o}, a_{s.o}) \vec{l}.\vec{s} \tag{1.3}$$

where $V_c(r)$ is the Coulomb potential due to a uniformly charged sphere, and

$$f(r, R, a) = \frac{1}{1 + \exp\left\{\frac{r-R}{a}\right\}} \tag{1.4}$$

with $V_o \approx 50$ MeV, $V_{s.o} \approx 5$ MeV, and typically $R_n \approx R_{s.o} \approx 1.2A^{1/3}$ fm and $a_n \approx a_{s.o} \approx 0.70$ fm [3].

1.3 Collective Models

An extreme form of the shell model is the independent particle model in which the nucleons move independently of each other in a common potential well. Correlations can

then be built up by introducing the nucleon-nucleon interaction. At the other extreme these correlations are introduced at the outset by considering collective nuclear motion, in which many nucleons contribute cooperatively to the nuclear properties. Thus nuclei with $A \approx 110$ are generally treated in terms of a model based on vibrations about a spherical equilibrium shape, while nuclei with A between 150 and 190 show structures more characteristic of rotations of nonspherical systems. These vibrations and rotations are the two major types of collective nuclear motion.

1.3.1 Vibrational Model

The vibrational model compares the nuclear vibrations to a liquid drop vibrating at high frequency. Although the average shape is spherical, the instantaneous shape is not. The instantaneous radial coordinate $R(t)$ of a point on the nuclear surface at (θ, ϕ) may be given in terms of the spherical harmonics $Y_{l\lambda}(\theta, \phi)$ with an amplitude $\alpha_{l\lambda}(t)$ such that

$$R(t, \theta, \phi) = R_o \left[1 + \sum_{l\lambda} \alpha_{l\lambda}(t) Y_{l\lambda}(\theta, \phi) \right]. \tag{1.5}$$

Modes with $l = 0$ and $l = 1$ are forbidden. The case with $l = 0$, known as the breathing mode, corresponds to a radial dependence on time only. The nucleus expands and contracts with a certain frequency. As nuclear matter is highly incompressible, such a vibrational mode requires a high excitation energy, and no low-lying breathing mode is expected. Also, a $l = 1$ vibration, known as a dipole vibration, produces a net displacement of the centre of mass and therefore is not possible in an isolated system [4]. The spectra resulting from the vibrational modes $l \geq 2$ are equally spaced with separation

$$\Delta E_l = \hbar \sqrt{\frac{C_l}{B_l}} \tag{1.6}$$

where B_l and C_l are the inertial and spring constants, respectively. ΔE_l increases with multipolarity l. In analogy with the quantum theory of electromagnetism, in which a unit of electromagnetic energy is called a photon, a quantum of vibrational energy is called a phonon. A single unit of $l = 2$ nuclear vibration is thus a quadrupole phonon [4].

1.3.2 Rotational Model

Nuclei in mass range $150 < A < 190$ and $A > 220$, are found to have substantial permanent distortions from spherical shape and are often called deformed nuclei. A common representation of the shape of these nuclei is that of an ellipsoid of revolution, the surface of which is described in a body fixed frame of reference by

$$R(\theta, \phi) = R_{av} \left[1 + \beta Y_{20}(\theta, \phi)\right] \tag{1.7}$$

which is independent of ϕ and therefore gives the nucleus cylindrical symmetry. The deformation parameter β is related to the eccentricity of the ellipse as

$$\beta = \frac{4}{3}\sqrt{\frac{\pi}{5}}\frac{\Delta R}{R_{av}} \tag{1.8}$$

where ΔR is the difference between the semimajor and semiminor axes of the ellipse and approximately $R_{av} = r_o A^{\frac{1}{3}}$. These nuclei are able to rotate about an axis perpendicular to the symmetry axis with kinetic energy $\frac{1}{2}I\omega^2$, where I is the moment of inertia about the axis of rotation, most simply assumed constant for the states in a given band.
In terms of the angular momentum $L = I\omega$, the energy is $L^2/2I$. Thus taking the quantum mechanical value of L^2 with L the angular momentum quantum number, gives $E = \dfrac{\hbar^2}{2I}L(L+1)$ for the energies of a rotating object in quantum mechanics. Increasing the quantum number L corresponds to adding rotational energy to the nucleus and the nuclear excited states form a sequence known as a rotational band [2]. For an even-even nucleus, axial symmetry about a body-fixed axis, together with reflectional invariance in the plane perpendicular to that axis of symmetry, yields a ground state band with
$L^\pi = 0^+, 2^+, 4^+, ...$ and the following sequence of excitation energies
$E(0^+) = 0$, $E(2^+) = 6(\hbar^2/2I)$, $E(4^+) = 20(\hbar^2/2I)$, $E(6^+) = 42(\hbar^2/2I)$,...
A typical mode of decay of these states is by electromagnetic $E2$ transitions in which a state of angular momentum L decays to the next lower state with angular momentum $(L-2)$, with the emission of a photon of quadrupole radiation.

Chapter 2

Cluster Model

The cluster model of the atomic nucleus treats nuclei as being composed of clusters with each cluster a spatially localised subsystem composed of nucleons with strongly correlated motions. Hence the cluster model is most appropriate when the clustering correlation becomes so strong that the relative motion between clusters becomes the fundamental mode of motion of the nucleus [5]. A particularly simple form of the cluster model, which we assume throughout this work, deals with a binary cluster system composed of a (heavy) core and (light) cluster.

2.1 Cluster-Core Decomposition

The core-cluster decomposition of a nucleus [mass A, charge Z] refers to the partitioning of a nucleus into a core $[A_1, Z_1]$ and a cluster $[A_2, Z_2]$. The nucleus $[A, Z]$ is called the parent nucleus and the core $[A_1, Z_1]$ the daughter. Among the clustering correlations which act to form a spatially localised cluster, four body correlations are prominent because of the tightly bound nature of the α-cluster. More generally the binary cluster model of a given nucleus is characterised by an appropriate core-cluster decomposition. Most heavy nuclei undergo α decay but occasionally a decay with a more massive ejectile is observed together with the α decay. This suggests a multiplicity of core-cluster configurations for the parent nucleus. We thus see that in order to apply a binary cluster model to a nucleus [A, Z] it

is necessary to first specify a likely partition of the nucleus into a core $[A_1,\ Z_1]$ and cluster $[A_2,\ Z_2]$. A superposition of many such core-cluster configurations possibly exists and, in applications in which a single core-cluster partition is assumed, it is then necessary that the single partition provides a reasonable approximation to the underlying superposition of partitions. In this thesis we restrict ourselves to nuclei which can be partitioned into a doubly magic core plus a doubly magic α-cluster, with the expectation that the greater than average stability of both core and cluster provides some justification for our restriction to a single partition.

2.2 Cluster-Core Interaction

In the binary cluster model the Hamiltonian separates into terms corresponding to the centre of mass and relative motion. The Schrödinger equation for the relative motion is given by

$$\hat{H}\psi(\vec{r}) = \left[-\frac{\hbar^2}{2\mu}\nabla^2 + V(\vec{r})\right]\psi(\vec{r}) = E\psi(\vec{r}) \tag{2.1}$$

where $\mu = \dfrac{A_1 A_2}{A_1 + A_2}$ is the reduced mass and $V(\vec{r})$ is the core-cluster interaction.
Replacing the total kinetic energy by its radial and rotational components and considering a central interaction composed of nuclear and Coulomb parts $V(\vec{r}) = V(r) = V_N(r) + V_c(r)$, equation (2.1) separates into radial and angular parts. Thus, substituting $\psi(\vec{r}) = \dfrac{1}{r}\varphi_{nL}(r)Y_{LM}(\theta,\phi)$, we find

$$\left[-\frac{\hbar^2}{2\mu}\frac{1}{r}\frac{d^2}{dr^2}r + \frac{\vec{l^2}}{2\mu r^2} + V(r)\right]\frac{\varphi_{nL}(r)}{r}Y_{LM}(\theta,\phi) = E_{nL}\frac{\varphi_{nL}(r)}{r}Y_{LM}(\theta,\phi) \tag{2.2}$$

where n is the number of nodes in the radial wavefunction, l is the angular momentum operator and L is the angular momentum eigenvalue. Using the eigenvalue equation for the angular momentum operator
$\vec{l^2}Y_{LM}(\theta,\phi) = \hbar^2 L(L+1)Y_{LM}(\theta,\phi)$, premultiplying by $Y^*_{LM}(\theta,\phi)$ and integrating over the angles, leads to the radial Schrödinger equation:

$$\left[-\frac{\hbar^2}{2\mu}\frac{d^2}{dr^2} + \frac{\hbar^2 L(L+1)}{2\mu r^2} + V(r)\right]\varphi_{nL}(r) = E_{nL}\varphi_{nL}(r). \tag{2.3}$$

Various forms of the nuclear potential $V_N(r)$ are considered in the following subsections. For the Coulomb potential $V_c(r,R)$ we take the form appropriate to a uniformly charged

spherical core (radius R_c) and a point cluster,

$$V_c(r) = \begin{cases} \frac{Z_1 Z_2 e^2}{2R_c}\left[3 - (\frac{r}{R_c})^2\right], & r \leq R_c \\ \frac{Z_1 Z_2 e^2}{r}, & r \geq R_c \end{cases} \tag{2.4}$$

To reduce the number of variables in the potential the nuclear and the Coulomb potential radii are set as equal, so $R_c = R$.

In the development of the binary cluster model, various forms for the nuclear potential have been used. In this chapter we consider three forms of nuclear potential $V_N(r, R)$; a square well potential, a cosh based potential and a Saxon Woods plus Saxon Woods cubed potential. Of these the SW + SW^3 form has proved most successful and will be the form used in our applications.

2.2.1 Square-Well Potential

The core-cluster interaction is assumed to be described by a square well nuclear form + (surface-charge) Coulomb form:

$$V = \begin{cases} -V_N + \frac{C}{R}, & r < R \\ C/r, & r > R \end{cases} \tag{2.5}$$

where V_N is the depth of the nuclear potential, which acts out to some distance R and $C = Z_1 Z_2 e^2$ is the product of the charges of core and cluster. This very simple parametrization which introduces the smallest number of parameters has been used by Buck et *al.* [6, 7] to achieve good agreement with a large set of α-decay half-lives in strong support of their alpha cluster model.

2.2.2 Cosh Potential

This is a form of nuclear potential which is given by

$$V_N(r) = -V_o \frac{1 + \cosh(R/a)}{\cosh(r/a) + \cosh(R/a)} \tag{2.6}$$

where V_o is the depth of the potential, R its radius, and a its diffuseness. For large R/a this potential has a similar shape to the Saxon Woods nuclear potential described in section

1.2. This potential has been used [8] in an α cluster model to predict successfully the α-decay half-lives for favored transitions from nuclear ground states of many heavy nuclei, as well as the excitation energies and electromagnetic transition strengths of light nuclei.

2.2.3 Saxon Woods and Saxon Woods Cubed Potential

Although the square well and cosh potentials described above gave a good account of the α decays from the ground states of nuclei, they failed to reproduce the spectra of heavy nuclei such as ^{212}Po which could be modelled as closed shell + α. Buck et *al*. thus introduced a mixture of Saxon Woods and Saxon Woods cubed forms given by $V_N(r,R) = -V_o f(r,R,a,x)$ with

$$f(r,R,a,x) = \frac{x}{1+\exp[\frac{r-R}{a}]} + \frac{1-x}{\left\{1+\exp[\frac{r-R}{3a}]\right\}^3} \tag{2.7}$$

where in addition to the depth V_o, radius R, and diffuseness a, there is a further parameter x specifying the geometry of the nuclear potential. This cubic term produces a deeper and more rounded potential in the interior of the core. The values of V_o, a and x are fixed for all nuclei, but the radius R is fitted separately for each nucleus. This form of nuclear potential has been used to describe simultaneously the low-lying positive parity spectrum and decay half-lives of ^{212}Po [9, 10].

2.3 Core-Cluster Orbit Quantum Number

The Pauli principle prohibits the nucleons in the cluster from occupying the same states as the nucleons in the core. The cluster model approximates this effect by ensuring appropriately surface peaked core-cluster wavefunctions by a suitable choice of the global quantum number $G = 2n + L$, which characterises the band with $J^\pi = L^\pi = 0^+, 2^+, 4^+, ...G^+$. As in Eq.(2.3) above n is the number of nodes in the wavefunction and L is the angular momentum of a state in the G-band. The Wildermuth condition, which maintains the total number of oscillator quanta independently of the mode of partition of the system, can be used to estimate a value for G. However, this condition is only a guide, in that the simple harmonic oscillator description neither takes into account the spin-orbit interaction which

significantly shifts the single-particle energies, nor the variation in the oscillator frequencies of core and cluster due to their large mass difference. Based roughly on the Wildermuth condition, Buck et *al*. have used a simple prescription of G for heavy nuclei, scaling it with the cluster mass such that $G = gA_2$ where $g = 5$ in the actinide region and $g = 4$ for the rare earth region [11-13]. Other investigations have been done to estimate the value of G. For example when applying the binary cluster model to superdeformation, and using a symmetric form of the core-cluster interaction, an expression for G has been developed [14] by examining the scaling with A_1A_2 of the Bohr-Sommerfeld quantization rule. This yields

$$G = \frac{0.88A_1A_2}{(A_1 + A_2)^{2/3}} = 0.88\mu(A_1 + A_2)^{1/3} \tag{2.8}$$

where G is rounded off to the nearest even integer.

A particular value of $G = 2n + L$ characterizes a band of states, for example the $L^\pi = 0^+, 2^+, 4^+...G^+$ ground state band of an even-even nucleus. For the states belonging to such a band we may rewrite Eq. (2.3) as

$$\left[-\frac{\hbar^2}{2\mu}\frac{d^2}{dr^2} + \frac{\hbar^2 L(L+1)}{2\mu r^2} + V(r)\right]\varphi_{GL}(r) = E_{GL}\varphi_{GL}(r). \tag{2.9}$$

Chapter 3

Spectra and Decays: Mathematical Framework

The binding energies of nuclear systems are typically of the order of MeV, whereas those encountered in atomic systems are of the order of keV. Thus the nucleus appears inert in everyday circumstances involving energies on the atomic scale. Nevertheless nuclear effects are of paramount importance in understanding physical process that occur at sufficiently high energies, as for example the mechanisms of energy release by stars, as well as the subsequent evolution of the abundance of atomic species in the universe. The advent of powerful particle accelerators in the second half of the 20^{th} century allowed greater control of the types of nuclear structure that could be studied, and resulted in an extensive nuclear data base [15].

In this chapter we discuss the mathematical framework that will enable us to generate binary cluster predictions of some nuclear observables such as excitation energies, electromagnetic transition rates, and α decay half-lives, and to compare these predictions with measured quantities in later chapters.

3.1 Bohr-Sommerfeld Quantization Rule

We first consider the semi-classical Wentzel-Kramers-Brillouin (WKB) approximation for the motion of a single particle of mass μ in a one dimensional potential $V(x)$ with SWE

$$\left[-\frac{\hbar^2}{2\mu}\frac{d^2}{dx^2} + V(x)\right]\varphi(x) = E\varphi(x), \tag{3.1}$$

with general solutions given by

$$\varphi(x) = \frac{A_+}{\sqrt{p(x)}}\exp\left[\frac{i}{\hbar}\int^x p(x^{'})dx^{'}\right] + \frac{A_-}{\sqrt{p(x)}}\exp\left[-\frac{i}{\hbar}\int^x p(x^{'})dx^{'}\right] \tag{3.2}$$

for the classically allowed region $E > V(x)$ and

$$\varphi(x) = \frac{B_+}{\sqrt{|p(x)|}}\exp\left[\frac{1}{\hbar}\int^x |p(x^{'})|dx^{'}\right] + \frac{B_-}{\sqrt{|p(x)|}}\exp\left[-\frac{1}{\hbar}\int^x |p(x^{'})|dx^{'}\right] \tag{3.3}$$

for the forbidden regions $E < V(x)$. $A_\pm$ and $B_\pm$ are arbitrary constants and the subscripts $\pm$ indicate the respective directions as illustrated in Figure 3.1.
The WKB approximation is valid if the wavelength λ_0 of the particle is slowly varying [16, 17] so that

$$\left|\frac{d\lambda_0}{dx}\right| \ll 1 \tag{3.4}$$

with the de Broglie wavelength $\lambda_0(x)$ given by

$$\lambda_0(x) = \frac{2\pi\hbar}{p(x)} = \frac{2\pi\hbar}{\sqrt{2\mu(E - V(x))}}. \tag{3.5}$$

It however fails at the classical turning points x_1 and x_2 where the particle has a zero momentum with $V(x) = E$ (shown in Fig. 3.2).
This turning point problem is usually fixed by the WKB connection formulae in which the solutions for both the classically allowed and forbidden regions are connected by some approximation taken at each turning point. For instance the solutions at both sides of x_1 may be connected as follows [16, 18]

$$\frac{C}{2\sqrt{|p(x)|}}\exp\left[\frac{1}{\hbar}\int_{x_1}^x |p(x^{'})|dx^{'}\right] \to \frac{C}{\sqrt{|p(x)|}}\sin\left[\frac{1}{\hbar}\int_{x_1}^x p(x^{'})dx^{'} + \frac{\pi}{4}\right] \tag{3.6}$$

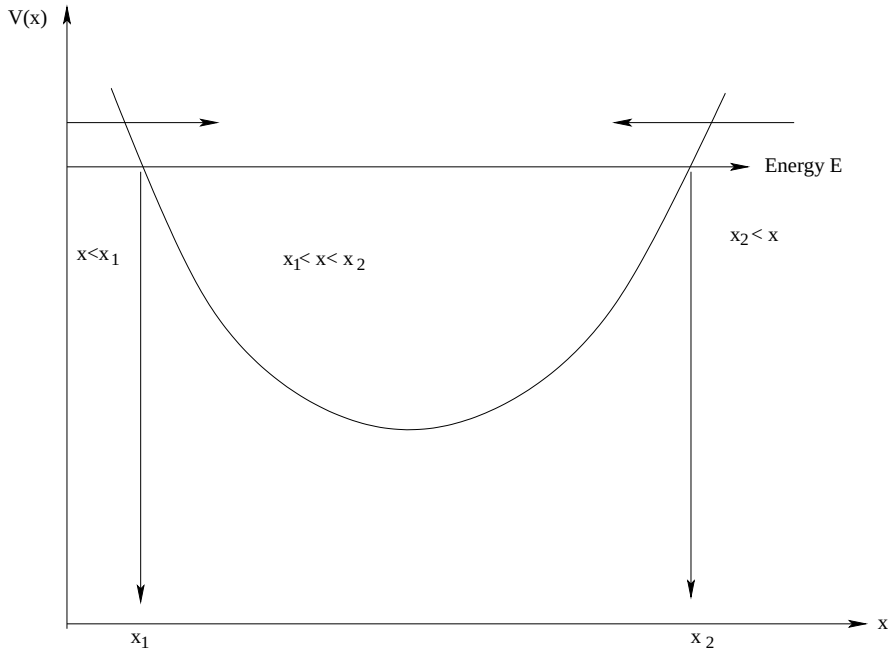

FIG. 3.1. Schematic of one dimensional potential $V(x)$ showing the different regions and the turning points x_1 and x_2. The arrows indicate the connection rule [18].

and similarly at x_2

$$\frac{D}{\sqrt{|p(x)|}}\sin\left[\frac{1}{\hbar}\int_x^{x_2} p(x^{'})dx^{'}+\frac{\pi}{4}\right] \leftarrow \frac{D}{2\sqrt{|p(x)|}}\exp\left[\frac{1}{\hbar}\int_x^{x_2}|p(x^{'})|dx^{'}\right] \tag{3.7}$$

where C and D are arbitrary constants and the arrows imply that the solutions at the tail continues into the solution at the arrow head for regions on the opposite sides of turning points but not vice-versa.

Combining the oscillatory solutions in the classically allowed region in equations (3.6 and 3.7) between x_1 and x_2 gives the well known Bohr-Sommerfeld (BS) quantization integral for a one dimensional system [16, 17];

$$\int_{x_1}^{x_2}\sqrt{\frac{2\mu}{\hbar^2}[E-V(x)]dx} = (2n+1)\frac{\pi}{2} \tag{3.8}$$

where n is the number of nodes.

The similarity of Eqs. (2.3) and (3.1) leads to a generalization of Eq.(3.8) to the three

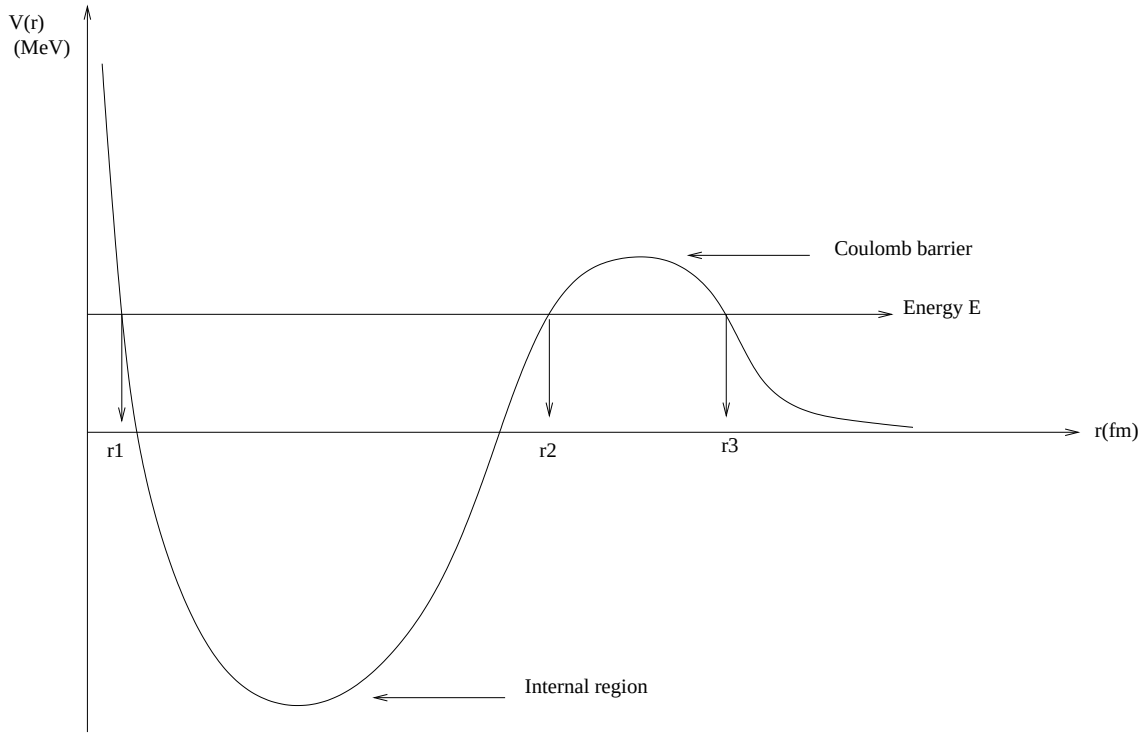

FIG. 3.2. A schematic plot of the potential $V(r)$ against the core-cluster separation distance r. The turning points r_1, r_2 and r_3 where $E = V(r)$ are shown for a typical quasibound state [18].

dimensional case given by

$$\int_{r_1}^{r_2} \sqrt{\frac{2\mu}{\hbar^2}[E - V(r)]dr} = (2n+1)\frac{\pi}{2} = (G - L + 1)\frac{\pi}{2} \tag{3.9}$$

where r_1, r_2 are the innermost classical turning points respectively in order of increasing distance from the origin, and the potential $V(r)$ contains nuclear, Coulomb and Langer-modified centrifugal terms

$$V(r) = V_N(r) + V_C(r) + \frac{\hbar^2}{2\mu r^2}\left(L + \frac{1}{2}\right)^2 \tag{3.10}$$

with $L\,(L+1)$ replaced by $\left(L + \frac{1}{2}\right)^2$.

3.2 $B\,(El)$ Values

Transitions between an initial state $\psi_i(\vec{r_1}, \vec{r_2}, ...\vec{r_A})$ and a final state $\psi_f(\vec{r_1}, \vec{r_2}, ...\vec{r_A})$ of a nucleus accompanied by the emission or absorption of radiation occur as a consequence of the coupling between an electromagnetic field and the charges and magnetic moments of the nucleons within the nucleus.
The probability of an electric transition is related to the transition strength $B(El)$ and is induced by an operator

$$\hat{B}_{lm}(El) = \sum_i q_i r_i^l Y_{lm}^*(\theta_i, \phi_i) \tag{3.11}$$

where l is the angular momentum transfer between the field and the system of charges q_i [19, 20].
In the following we concentrate mainly on electric transitions between states of a band with $L^\pi = 0^+, 2^+, 4^+...G^+$. Dropping explicit reference to the band index G we use the shorthand notation for these states

$$|LM\rangle = \psi_{LM}(\vec{r}) = \frac{\varphi_L(r)}{r} Y_{LM}(\theta, \phi), \tag{3.12}$$

where $\varphi_L(r)$ is a solution of the radial Schrödinger equation (see Eq. 2.9).

For a transition of order l from an initial state $|L_i M_i\rangle = |lm\rangle$ to a spinless final state $|L_f M_f\rangle = |00\rangle$, for instance the ground state of an even-even nucleus, the transition strength $B(El; l \to 0^+)$ is given by

$$\begin{aligned} B(El; l \to 0^+) &= |\langle \psi_{00} | \hat{B}_{lm}(El) | \psi_{lm} \rangle|^2 \\ &= |\langle \psi_{00} | \sum_i q_i r_i^l Y_{lm}^*(\theta_i, \phi_i) | \psi_{lm} \rangle|^2. \end{aligned} \tag{3.13}$$

In a binary cluster model of the nucleus, the core and the cluster correspond to two charge distributions Z_1 and Z_2 so that Eq. (3.11) can be rewritten

$$\hat{B}_{lm}(El) = Z_1 r_1^l Y_{lm}^*(\theta_1, \phi_1) + Z_2 r_2^l Y_{lm}^*(\theta_2, \phi_2). \tag{3.14}$$

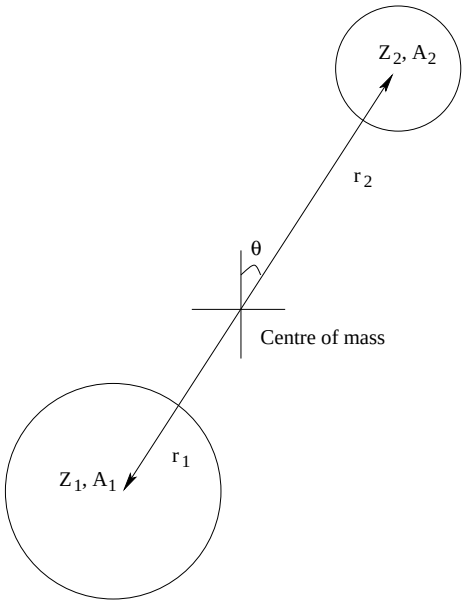

FIG. 3.3. Schematic representation of the core-cluster coordinates of relative motion [19].

In the centre of mass frame (see Fig. 3.3), converting to the relative coordinate r with $r_1 = A_2 r/A$ and $r_2 = A_1 r/A$, we have

$$\begin{aligned}
\hat{B}_{lm}(El) &= Z_1 r_1^l Y_{lm}^*(\theta_1,\phi_1) + Z_2 r_2^l Y_{lm}^*(\theta_2,\phi_2) \\
&= Z_1 r_1^l Y_{lm}^*(\pi-\theta,\pi+\phi) + Z_2 r_2^l Y_{lm}^*(\theta,\phi) \\
&= \left[(-1)^l Z_1 r_1^l + Z_2 r_2^l\right] Y_{lm}^*(\theta,\phi) \\
&= \left[Z_1\left(\frac{-A_2 r}{A}\right)^l + Z_2\left(\frac{A_1 r}{A}\right)^l\right] Y_{lm}^*(\theta,\phi) \\
&= \left[Z_1\left(\frac{-A_2}{A}\right)^l + Z_2\left(\frac{A_1}{A}\right)^l\right] r^l Y_{lm}^*(\theta,\phi). \qquad (3.15)
\end{aligned}$$

Inserting (3.15) into (3.13)

$$\begin{aligned}
B_{lm}(El) &= \frac{1}{4\pi}\left|\langle\frac{\varphi_0(r)}{r}\right| \left\{Z_1\left(\frac{-A_2}{A}\right)^l + Z_2\left(\frac{A_1}{A}\right)^l\right\} r^l Y_{lm}^*(\theta,\phi) \left|\frac{\varphi_l(r)}{r} Y_{lm}(\theta,\phi)\rangle\right|^2 \\
&= \frac{1}{4\pi}\left|\int_0^\infty \frac{\varphi_0^*(r)}{r}\left\{Z_1\left(\frac{-A_2}{A}\right)^l + Z_2\left(\frac{A_1}{A}\right)^l\right\} r^l \frac{\varphi_l(r)}{r} r^2 dr\right|^2. \qquad (3.16)
\end{aligned}$$

We note that the transition probabilities decrease rapidly with multipolarity [1, 19]. The multipolarities of most interest are the dipole (l=1) and the quadrupole (l=2) transitions respectively.

3.2.1 Dipole Transitions

These involve transitions with l=1 between states of opposite parities. For a spinless final state the binary cluster $B(E1)$ value is given by

$$B(E1;1^- \rightarrow 0^+) = \frac{1}{4\pi}\left|\left\{Z_1\left(\frac{-A_2}{A}\right)+Z_2\left(\frac{A_1}{A}\right)\right\}\int_0^\infty \varphi_0^*(r)r\varphi_1(r)dr\right|^2. \tag{3.17}$$

It is known that the $B(E1)$ between low-lying states are very small for heavy nuclei [21] and hence

$$Z_1\left(\frac{-A_2}{A}\right)+Z_2\left(\frac{A_1}{A}\right)\approx 0 \tag{3.18}$$

which gives the important no dipole condition [46, 51]

$$\frac{Z_1}{A_1}=\frac{Z_2}{A_2}=\frac{Z}{A} \tag{3.19}$$

with $A = A_1 + A_2$ and $Z = Z_1 + Z_2$.

3.2.2 Quadrupole Transitions

These involve transitions with $l = 2$ between states of the same parity. For a spinless final state the binary cluster $B(E2)$ value is given by

$$B(E2;2^+ \rightarrow 0^+) = \frac{1}{4\pi}\left|\left[Z_1(\frac{-A_2}{A})^2+Z_2(\frac{A_1}{A})^2\right]\int_0^\infty \varphi_0^*(r)r^2\varphi_2(r)dr\right|^2. \tag{3.20}$$

Applying the no dipole condition given in Eq. (3.19), we can write

$$\begin{aligned} Z_1\left(\frac{A_2}{A}\right)^2+Z_2\left(\frac{A_1}{A}\right)^2 &= Z_1\left(\frac{Z_2}{Z}\right)\left(\frac{A_2}{A}\right)+Z_2\left(\frac{Z_1}{Z}\right)\left(\frac{A_1}{A}\right) \\ &= \frac{Z_1Z_2}{Z}\left(\frac{A_1+A_2}{A}\right) \\ &= \frac{Z_1Z_2}{Z} \end{aligned} \tag{3.21}$$

and thus

$$B(E2;2^+ \rightarrow 0^+) \approx \frac{1}{4\pi}\left|\frac{Z_1Z_2}{Z}\int_0^\infty \varphi_0^*(r)r^2\varphi_2(r)dr\right|^2. \tag{3.22}$$

For heavy nuclei, the cluster model results in multinodal radial wavefunctions φ_0 and φ_2 very similar in the important surface region [22] so that

$$\begin{aligned} B(E2; 2^+ \to 0^+) &\approx \frac{1}{4\pi} \left| \frac{Z_1 Z_2}{Z} \int_0^\infty \varphi_0^*(r) r^2 \varphi_0(r) dr \right|^2 \\ &\approx \frac{1}{4\pi} \left| \frac{Z_1 Z_2}{Z} r_0^2 A^{2/3} \right|^2 \end{aligned} \tag{3.23}$$

with $r_0 \sim 1.1$ fm.

3.2.3 Reduced Probability for Arbitrary Transitions

For an electric transition of multipolarity l from an arbitrary initial state $|L_i M_i\rangle$ to an arbitrary final state $|L_f M_f\rangle$ we must average over the angular momentum projections M_i of the initial states, and sum over the corresponding M_f of the final states. Use of the Wigner-Eckart theorem and the orthogonality relation of the Clebsch-Gordon coefficients [15, 18] then results in a transition strength given by:

$$\begin{aligned} B\left(El; L_i \to L_f\right) &= \sum_{m M_f} |\langle L_f M_f | \hat{B}_{lm}(El) | L_i M_i \rangle|^2 \\ &= \sum_{m M_f} |\langle L_f M_f | \beta_l r^l Y_{lm}^*(\theta, \phi) | L_i M_i \rangle|^2 \\ &= \sum_{m M_f} |(-1)^m \langle L_f M_f | \beta_l r^l Y_{l-m}(\theta, \phi) | L_i M_i \rangle|^2 \\ &= \sum_{m M_f} |\langle L_i M_i l - m | L_f M_f \rangle|^2 |\langle L_f \| \beta_l r^l Y_l \| L_i \rangle|^2 \\ &= \sum_{m M_f} \frac{2L_f + 1}{2L_i + 1} |\langle L_f M_f l m | L_i M_i \rangle|^2 |\langle L_f \| \beta_l r^l Y_l \| L_i \rangle|^2 \\ &= \frac{2L_f + 1}{2L_i + 1} |\langle L_f \| \beta_l r^l Y_l \| L_i \rangle|^2 \\ &= \left(\frac{\hat{L_f}}{\hat{L_i}} \right)^2 |\langle L_f \| \beta_l r^l Y_l \| L_i \rangle|^2 \end{aligned} \tag{3.24}$$

with $\beta_l = \left[Z_1 \left(\frac{-A_2}{A} \right)^l + Z_2 \left(\frac{A_1}{A} \right)^l \right]$ and $\hat{L} = \sqrt{2L+1}$.

From Eq. (3.12), evaluating the reduced matrix element [23], we have

$$\begin{aligned} B\left(El; L_i \to L_f\right) &= \frac{1}{4\pi} \left(\frac{\hat{L_f}}{\hat{L_i}} \right)^2 \left(\frac{\hat{L_i}\hat{l}}{\hat{L_f}} \langle L_i 0 l 0 | L_f 0 \rangle \right)^2 |\langle \varphi_{L_f} | \beta_l r^l | \varphi_{L_i} \rangle|^2 \\ &= \beta_l^2 \left(\frac{l^2}{4\pi} \right) \left(\langle L_i 0 l 0 | L_f 0 \rangle \right)^2 |\langle \varphi_{L_f} | r^l | \varphi_{L_i} \rangle|^2. \end{aligned} \tag{3.25}$$

For a transition involving a final state with $L_f = 0^+$ we then have $L_i = l$ and (3.25) reduces to

$$B(El; L_i \to 0^+) = \beta_l^2 \left(\frac{1}{4\pi} \right) |\langle \phi_0 | r^l | \phi_l \rangle|^2 \tag{3.26}$$

in agreement with the directly obtained result (3.16).

Rather than expressing transition strengths in units of $e^2 fm^{2l}$ as has been assumed in section 3.2, we may express them in Weisskopf single particle units (W.u). The latter refer to a nuclear system composed of a single proton, having initial and final wavefunction with constant radial dependence throughout the nuclear volume. This results in the conversion factor

$$B(El) \text{ (W.u)} = \frac{1}{4\pi} \left[\frac{3}{(l+3)} r_0^l A^{l/3} \right]^2 e^2 fm^{2l} \tag{3.27}$$

3.3 Alpha Decay

Many heavy nuclei, and in particular those of a naturally occurring radioactive series, decay through α emission. α-particles were first identified as the least penetrating of the radiations emitted by naturally occuring materials. In 1903, Rutherford measured their charge-to-mass ratio by deflecting α particles from the decay of radium in an electric and magnetic field. In 1909, Rutherford showed that, as suspected, the α particles were in fact helium nuclei [1].

Alpha emission becomes increasingly important for heavy nuclei due to the repulsive Coulomb force which, because of its long range, increases with size at faster rate than does the short range nuclear attraction [2].

Alpha emission is spontaneous in that some kinetic energy suddenly appears in the system for no apparent cause, accompanied by a decrease in the mass of the system. This

spontaneous emission of an α particle can be represented by: ${}^{A}_{Z}X_N \longrightarrow {}^{A-4}_{Z-2}X'_{N-2} + \alpha$. Conservation of energy gives: $m_X c^2 = m_{X'}c^2 + T_{X'} + m_\alpha c^2 + T_\alpha$
or $(m_X - m_{X'} - m_\alpha)c^2 = T_{X'} + T_\alpha$. This quantity is equal to the net energy released in the decay, called the Q value; $Q = (m_X - m_{X'} - m_\alpha)c^2$ or $Q = T_{X'} + T_\alpha$.
The possibility of emission of particles heavier than alpha-particles was first considered in 1980 by Sandulescu *et al.* [16].

3.3.1 Alpha Decay Constant and Half-Life

In 1928, Gamov, Gurney and Condon developed almost simultaneously a quantum mechanical theory of α emission. In this theory, an α particle is preformed inside the parent nucleus and is assumed to move in a spherical region determined by the daughter nucleus. The alpha particle within the nucleus presents itself again and again at the barrier surface until it finally penetrates. The disintegration constant of an alpha emitter is given in the one-body theory by $\lambda = fP$, where f is the frequency with which the alpha particle presents itself at the barrier and P is the probability of transmission through the barrier. Fig.3.2. shows that the quantity f is roughly equal to $v/2(r_2 - r_1)$.
A pure radioactive substance decreases with time according to an exponential law. If N radioactive nuclei are present at time t and if no new nuclei are introduced into the sample, then the number dN decaying in a time dt is proportional to N, and so

$$\lambda = -\frac{(dN/dt)}{N}. \tag{3.28}$$

Integrating this equation gives

$$N(t) = N_o e^{-\lambda t} \tag{3.29}$$

where N_o is the number of radioactive nuclei at $t = 0$.
The half-life $T_{1/2}$ gives the time necessary for half of the nuclei to decay. Plugging $N = N_o/2$ into Eq. (3.29) gives

$$T_{1/2} = \frac{ln2}{\lambda} = \frac{ln2}{fP}. \tag{3.30}$$

Semi-classically we find

$$\frac{1}{f} = \frac{2(r_2 - r_1)}{v} = \frac{2m(r_2 - r_1)}{p} = \frac{2m(r_2 - r_1)}{\hbar K} = \frac{2m}{\hbar}\int_{r_1}^{r_2}\frac{dr}{K} \tag{3.31}$$

where p and K are the momentum and wavenumber in the classically allowed region between r_1 and r_2.
The probability of tunneling through the barrier is given by the ratio of the probability densities at the edges of the barrier

$$\frac{(\psi\psi^*)transmitted}{(\psi\psi^*)incident}.$$

For an infinitely thick barrier only the exponentially decreasing term of the wavefunction persists. Taking the barrier to be large , the transmission probability is [24]

$$P = \exp\{-2k(r_3 - r_2)\} = \exp\left\{-2\int_{r_2}^{r_3} k dr\right\} \tag{3.32}$$

where k is the wavenumber in the region between r_2 and r_3. Thus

$$\mathrm{T}_{1/2} = \frac{2mln2}{\hbar}\left[\int_{r_1}^{r_2}\frac{dr}{K}\right]\left[\exp\left\{2\int_{r_2}^{r_3} k dr\right\}\right]. \tag{3.33}$$

In deriving Eq. (3.33) we have assumed constant wavenumbers K and k. In general the wavenumbers K and k are functions of r so that

$$\mathrm{T}_{1/2} = \frac{2mln2}{\hbar}\left[\int_{r_1}^{r_2}\frac{dr}{K(r)}\right]\left[\exp\left\{2\int_{r_2}^{r_3} k(r) dr\right\}\right]. \tag{3.34}$$

Thus, the decay constant is [19]

$$\lambda = \frac{ln2}{T_{1/2}} = \frac{\hbar}{2m}\frac{\exp\left\{-2\int_{r_2}^{r_3} k(r)dr\right\}}{\int_{r_1}^{r_2}[K(r)]^{-1}\,dr}, \tag{3.35}$$

a result which agrees with that obtained from a rigorous treatment of the decay [25]. The decay width Γ is given by $\Gamma = \hbar\lambda$.

One still needs to consider the preformation process. The probability $P^{'}$ of having a preformed cluster-core system in the initial state is poorly determined and the cluster model at its simplest assumes that the states of a given band are described by the relative motion of a core and cluster in their respective ground states, so that the probability $P^{'}$=1.

As decay is essentially a Coulomb barrier problem, the effect of the electron cloud as the ejectile escapes the atom is not negligible. Thus, the Q-value needs to be increased by the

electron shielding correction [26, 27]. This is important, particularly for exotic decay, in that the decays are very sensitive to relatively small variations in Q-value.

In the case of ^{212}Po, α-decay to the ground state of ^{208}Pb offers significant competition to $E2$ γ-decay. It is therefore more illuminating to evaluate $\alpha-$ and $\gamma-$decay widths Γ_α and Γ_γ and then to compute the half-lives and α-branching ratios for comparison with experimental values. The γ-decay width is related to $B(E2; L_i \rightarrow L_f)$ values by

$$\Gamma_\gamma = 8.070 \times 10^{-13} E_\gamma^5 (1 + \alpha_T) \times B(E2; L_i \rightarrow L_f, e^2 fm^4)[10] \tag{3.36}$$

where E_γ is the γ-ray energy in MeV, and α_T is the appropriate internal conversion coefficient [10].
In terms of the widths Γ_α and Γ_γ, the half-life $T_{1/2}$ and α-branching ratio b_α are given by

$$\mathrm{T}_{1/2} = \frac{\hbar \ln 2}{\Gamma_\alpha + \Gamma_\gamma} \tag{3.37}$$

and

$$\mathrm{b}_\alpha = \frac{\Gamma_\alpha}{\Gamma_\alpha + \Gamma_\gamma}. \tag{3.38}$$

3.3.2 Alpha Decay Spectroscopy

The alpha decay of the parent nucleus may leave the daughter in an excited state which in turn emits γ-rays as it decays to lower energy states. The nucleus excitation energy spectrum can then be determined from the energies of emitted γ-rays due to transitions between various α plus core states.

Chapter 4

Spectra and Decays: Comparison with Experiment

We next test the predictions of the model against measurements in the alpha plus closed shell systems ^{20}Ne, ^{44}Ti, ^{94}Mo, ^{136}Te and ^{212}Po in order to determine whether a particular form of the cluster-core potential is able to simultaneously describe such measurements. Concentrating on the ground state bands of these nuclei we find that although the square well, cosh, and SW potentials can give a reasonable account of much of the data on electromagnetic and α decays, only the SW + SW^3 form has been found to be able to simultaneously describe the excitation spectra. In particular, for the heavier nuclei, the square well, cosh, and SW potentials result in inverted spectra with the 0^+ member of the $L^\pi = 0^+, 2^+, 4^+, ...G^+$ ground state band at a higher energy than the G^+ member of the band [9].

The original form of the SW + SW^3 potential [10] is not symmetric with respect to the interchange of core and cluster. We thus use the more physical symmetric form introduced by Buck *et al.* [22].

$$V_N(r,R) = -\left(\frac{A_1 A_2}{A_1 + A_2 - 1}\right) U_0 \frac{f(r,R,a,x)}{f(0,R,a,x)} \tag{4.1}$$

where the function $f(r,R,a,x)$ as defined in Eq. (2.7). In Eq. (4.1) U_0 and a are kept fixed at their original values $U_0 = 54$ MeV and $a = 0.73$ fm [22], and x has been fine-tuned from its original value of $x = 0.33$ fm [22] to $x = 0.35$ fm.

We find that as we properly shape the potential in the internal region, we avoid the trend

to the inverted spectra and we can simultaneously predict well the energy levels, the α decay half-lives and the elastic scattering differential cross-sections.

For each nucleus the radius R of the α-core potential is determined by optimizing the fit of the theoretical to the experimental spectra of the ground state band. The Coulomb radius R_c is constrained to equal R in order to limit the number of free parameters. The fitting procedure can be implemented in semiclassical approximation without significant loss of accuracy and the energies of bound and quasibound states are obtained using the Bohr-Sommerfeld quantization rule in Eq. (3.9). For each nucleus we find R by minimising the expression

$$S_E = \sum_L \left[E_L^{expt}(MeV) - E_L^{calc}(MeV)\right]^2 \tag{4.2}$$

which fits the model predictions of the band energy spectrum to the corresponding experimental values.

4.1 Energy Levels

In Figs. 4.1 to 4.5 we compare potentials with $x = 0.35$ and $x = 1.0$ and note the more rounded form of the $x = 0.35$ potential. For heavy nuclei this results in upright rather than inverted spectra. In particular the level sequence and the compression of the higher spin states of ^{212}Po are well reproduced with the 16^+ state above the 18^+ state (see Table 4.1). This provides an explanation for the isomeric nature of the 18^+ state since the electromagnetic transition from this state is strongly hindered, with the decay of the state proceeding mainly through α emission, which is itself hindered by the large centrifugal barrier. Overall the calculated spectra for the nuclei investigated are in good agreement with experiment, as shown in Tables 4.1 to 4.5 (see Appendix D for graphic representations of these spectra).

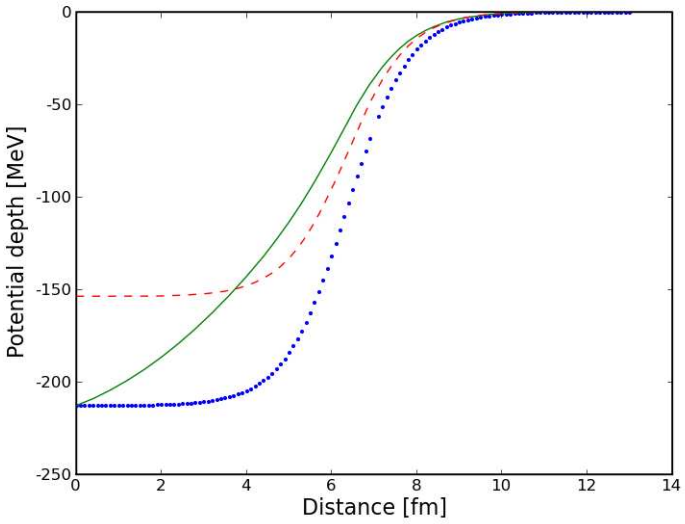

FIG. 4.1. Plot of the mass symmetric SW + SW^3 potential for ^{212}Po from Eq. (4.1) and parameter values $a = 0.73$ fm, $R = 6.35756$ fm and 1) $V_0 = 54$ MeV and $x = 0.35$ (solid line), 2) $V_0 = 54$ MeV and $x = 1.0$ (dotted line), and 3) $V_0 = 38$ MeV and $x = 1.0$ (dash line). Potentials 1) and 3) are fitted to $G = 18$.

TABLE. 4.1. Excitation energies of the low-lying positive parity states in ^{212}Po. Experimental values *Expt* E* (MeV) are compared with their calculated counterparts *Calc.* E* (MeV) obtained using $G = 18$ and the SW + SW^3 potential of Eq. (4.1) with $U_0 = 54$ MeV, $R = 6.35756$ fm, $a = 0.73$ fm, $x = 0.35$. The goodness of fit parameter of Eq. (4.2) $S_E = 1.14453$.

J^π	*Expt.* E*[MeV]	*Calc.* E*MeV
0^+	0.000	-0.070
2^+	0.727	0.159
4^+	1.133	0.569
6^+	1.356	1.101
8^+	1.476	1.698
10^+	1.834	2.303
12^+	2.702	2.843
14^+	2.855	3.228
16^+	-	3.343
18^+	2.922	2.997

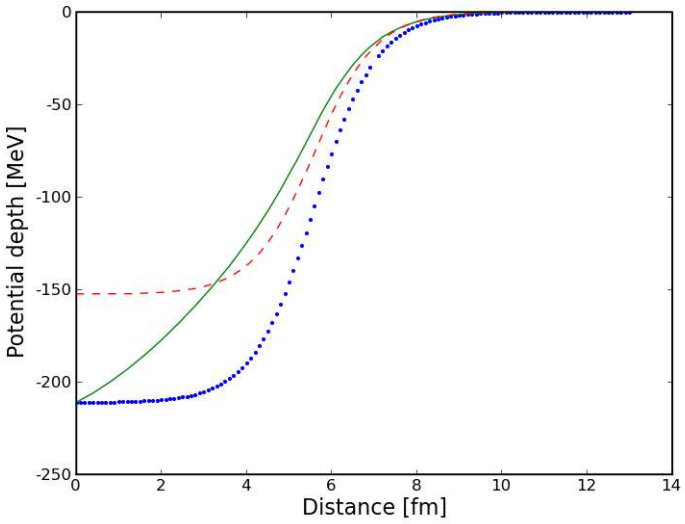

FIG. 4.2. Plot of the mass symmetric SW + SW^3 potential for ^{136}Te from Eq. (4.1) and parameter values $a = 0.73$ fm, $R = 5.59085$ fm and 1) $V_0 = 54$ MeV and $x = 0.35$ (solid line), 2) $V_0 = 54$ MeV and $x = 1.0$ (dot line), and 3) $V_0 = 38$ MeV and $x = 1.0$ (dash line). Potentials 1) and 3) are fitted to $G = 16$.

TABLE. 4.2. Excitation energies of the low-lying positive parity states in ^{136}Te. Experimental values *Expt.* E* (MeV) are compared with their calculated counterparts *Calc.* E* (MeV) obtained using G = 16 and the SW + SW^3 potential of Eq. (4.1) with $U_0 = 54$ MeV, $R = 5.59085$ fm, $a = 0.73$ fm, $x = 0.35$. The goodness of fit parameter of Eq. (4.2) $S_E = 2.26761$.

J^π	*Exp.* E*(MeV)	*Calc.* E*(MeV)
0^+	0.000	-0.440
2^+	0.606	-0.111
4^+	1.03	0.496
6^+	1.3826	1.288
8^+	2.1321	2.189
10^+	2.792	3.108
12^+	3.1871	3.929
14^+	3.7205	4.503

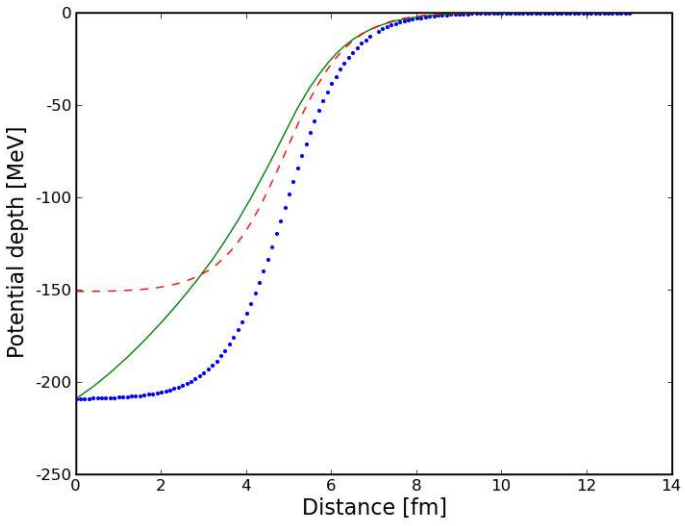

FIG. 4.3. Plot of the mass symmetric SW + SW^3 potential for ^{94}Mo from Eq. (4.1) and parameter values $a = 0.73$ fm, $R = 4.91241$ fm and 1) $V_0 = 54$ MeV and $x = 0.35$ (solid line), 2) $V_0 = 54$ MeV and $x = 1.0$ (dotted line), and 3) $V_0 = 39$ MeV and $x = 1.0$ (dash line). Potentials 1) and 3) are fitted to $G = 14$.

TABLE. 4.3. Excitation energies of the low-lying positive parity states in ^{94}Mo. Experimental values *Expt.* E* (MeV) are compared with their calculated counterparts *Calc.* E* (MeV) obtained using $G = 14$ and the SW + SW^3 potential of Eq. (4.1) with $U_0 = 54$ MeV, $R = 4.91241$ fm, $a = 0.73$ fm, $x = 0.35$. The goodness of fit parameter of Eq. (4.2) $S_E = 1.75017$.

J^π	*Exp.* E*(MeV)	*Calc.* E*(MeV)
0^+	0.000	-0.229
2^+	0.871	0.233
4^+	1.573	1.084
6^+	2.322	2.203
8^+	2.955	3.478
10^+	3.897	4.775

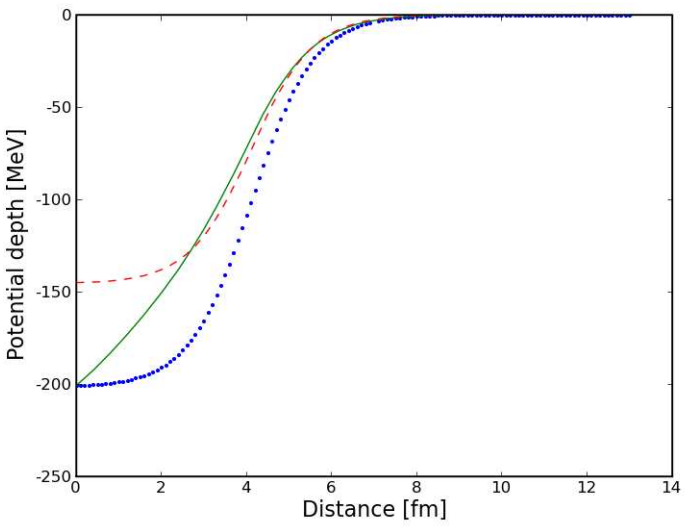

FIG. 4.4. Plot of the mass symmetric SW + SW^3 potential for ^{44}Ti from Eq. (4.1) and parameter values $a = 0.73$ fm, $R = 4.11498$ fm and 1) $V_0 = 54$ MeV and $x = 0.35$ (solid line), 2) $V_0 = 54$ MeV and $x = 1.0$ (dotted line), and 3) $V_0 = 39$ MeV and $x = 1.0$ (dash line). Potentials 1) and 3) are fitted to $G = 12$.

TABLE. 4.4. Excitation energies of the low-lying positive parity states in ^{44}Ti. Experimental values *Expt.* E* (MeV) are compared with their calculated counterparts *Calc.* E* (MeV) obtained using G = 12 and the SW + SW^3 potential of Eq. (4.1) with $U_0 = 54$ MeV, $R = 4.11498$ fm, $a = 0.73$ fm, $x = 0.35$. The goodness of fit parameter of Eq. (4.2) $S_E = 6.39933$.

J^π	*Exp.* E*(MeV)	*Calc.* E*(MeV)
0^+	0.000	-0.180
2^+	1.083	0.507
4^+	2.454	1.822
6^+	4.015	3.615
8^+	6.508	5.746
10^+	7.671	8.031
12^+	8.039	10.222

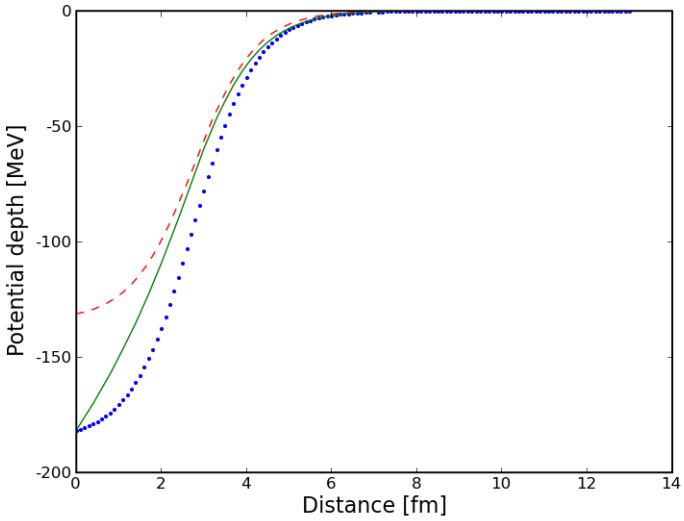

FIG. 4.5. Plot of the mass symmetric SW + SW^3 potential for ^{20}Ne from Eq. (4.1) and parameter values $a = 0.73$ fm, $R = 2.76188$ fm and 1) $V_0 = 54$ MeV and $x = 0.35$ (solid line), 2) $V_0 = 54$ MeV and $x = 1.0$ (dotted line), and 3) $V_0 = 39$ MeV and $x = 1.0$ (dash line). Potentials 1) and 3) are fitted to $G = 8$.

TABLE. 4.5. Excitation energies of the low-lying positive parity states in ^{20}Ne. Experimental values *Expt.* E* (MeV) are compared with their calculated counterparts *Calc.* E* (MeV) obtained using $G = 8$ and the SW + SW^3 potential of Eq. (4.1) with $U_0 = 54$ MeV, $R = 2.76188$ fm, $a = 0.73$ fm, $x = 0.35$. The goodness of fit parameter of Eq. (4.2) $S_E = 5.69784$.

J^π	*Exp.* E*(MeV)	*Calc.* E*(MeV)
0^+	0.000	-0.449
2^+	1.633	0.963
4^+	4.247	3.846
6^+	8.777	8.175
8^+	11.951	14.078

4.2 $B(\mathrm{E}2\downarrow)$ Values

We evaluate the B(E2 $\downarrow$) reduced transition strengths with the radial wave functions for each state obtained from a numerical solution of the Schrödinger wave equation using a potential given in Eq. (4.1) and without introducing any effective charges. The level of agreement between the theoretical calculations and the experimental data is genereally good to within a factor of ~ 2, with some measured values characterized by large uncertainties. Hopefully further measurements will reduce these uncertainties. The experimental as well as theoretical $B(E2\downarrow)$ results are given in Tables (4.7 - 4.10).

TABLE. 4.6. Experimental and theoretical electromagnetic transition strengths of ^{212}Po in Weisskopf units (W.u) obtained with the SW + SW^3 with G=18, R=6.35756 fm . The measured values are taken from [10].

J^π	$B(E2\downarrow)$exp(W.u)	$B(E2\downarrow)$calc(W.u)
0^+	-	-
2^+	-	3.8
4^+	-	5.3
6^+	3.9 ± 1.1	5.4
8^+	2.3 ± 0.1	5.1
10^+	2.2 ± 0.6	4.5
12^+	-	3.7
14^+	-	2.8

TABLE. 4.7. Experimental and theoretical electromagnetic transition strengths of ^{94}Mo in e^2fm^4 obtained with the SW + SW^3 with G=14, R=4.91241 fm . The measured values are taken from [10].

J^π	B($E2\downarrow$)exp(e^2fm^4)	B($E2\downarrow$)calc(e^2fm^4)
0^+	-	-
2^+	391 ± 5	163
4^+	660 ± 101	225
6^+	-	232
8^+	-	219
10^+	-	194

TABLE. 4.8. Experimental and theoretical electromagnetic transition strengths of ^{44}Ti in e^2fm^4 obtained with the SW + SW^3 with G=12, R=4.11498 fm . The measured values are taken from [10].

J^π	B($E2\downarrow$)exp(e^2fm^4)	B($E2\downarrow$)calc(e^2fm^4)
0^+	-	-
2^+	120 ± 37	94
4^+	277 ± 37	128
6^+	157 ± 28	123
8^+	> 14	101
10^+	138 ± 28	69
12^+	< 60	34

TABLE. 4.9. Experimental and theoretical electromagnetic transition strengths of ^{20}Ne in e^2fm^4 obtained with the SW + SW^3 with G=8, R=2.76188 fm . The measured values are taken from [10].

J^π	B($E2\downarrow$)exp(e^2fm^4)	B($E2\downarrow$)calc(e^2fm^4)
0^+	-	-
2^+	68 ± 4	40
4^+	71 ± 7	52
6^+	65 ± 10	44
8^+	30 ± 4	24

4.3 α decay Half-lives and α Branching Ratios of ^{212}Po

Using the values of the widths from Table (4.10), we calculate $T_{1/2}$ and b_α, and in Table (4.11) compare our results with the corresponding experimental values. For the half-lives $T_{1/2}$ the agreement is generally good and this enables us to make confident predictions of $T_{1/2}$ for the 2^+ and 4^+ members of the band. Only the 18^+ half-life prediction lies a factor ~ 3 from the corresponding measurement. The agreement with the measured values for the branching ratios is very good by a factor ~ 1.

TABLE. 4.10. The calculated Γ_γ(MeV) and Γ_α(MeV) decay widths of ^{212}Po using the SW + SW^3 potential of Eq. (4.1) with parameter values specified in Table 4.1. The total internal conversion factor (α_T) values are taken from [10, 18]. The asterisks denote that theoretical estimates for (α_T) have been used.

J^π	$E^*(MeV)$	α_T	Γ_γ(MeV)	Γ_α(MeV)
0^+	0.000	-	-	7.612×10^{-16}
2^+	0.727	0.014	4.741×10^{-11}	1.834×10^{-14}
4^+	1.133	0.055	3.737×10^{-12}	3.222×10^{-14}
6^+	1.356	0.340	2.398×10^{-13}	1.073×10^{-14}
8^+	1.476	3.400	3.314×10^{-14}	1.062×10^{-15}
10^+	1.834	0.076	1.727×10^{-12}	1.428×10^{-16}
12^+	2.702	0.0097*	1.115×10^{-10}	6.953×10^{-17}
14^+	2.885	0.650*	7.592×10^{-14}	9.919×10^{-19}
16^+	-	-	-	-
18^+	2.922	-	-	3.375×10^{-24}

TABLE. 4.11. α decay half-lives $T_{1/2}$ and alpha branching ratios b_α for the ground states of ^{212}Po. Comparison of the experimental $T_{1/2}$(expt) and theoretical $T_{1/2}(theor.)$ half-lives, the experimental b_α(expt) and theoretical $b_\alpha(theor.)$ alpha branching ratios, respectively. The asterisks denote that theoretical estimates of total internal conversion factors have been used. The b_α(expt) values are taken from [28].

J^π	$E^*(MeV)$	$T_{1/2}$(expt)	$T_{1/2}(theor.)$	b_α (%)$(exp.)$	b_α(%)$(theor.)$
0^+	0.000	$0.30\mu s$	$0.599\mu s$	100	100
2^+	0.727	-	9.618ps	0.033	0.038
4^+	1.133	-	0.121ns	~ 0.5	0.855
6^+	1.356	0.76 ± 0.21ns	1.807ns	$\sim 3 \pm 1$	4.249
8^+	1.476	17ns	13.340ns	$\sim 3 \pm 1$	3.105
10^+	1.834	$0.55 \pm 0.14ns$	0.264ns	-	0.008
12^+	2.702	-	4.091*ps	-	6.234×10^{-5}
14^+	2.885	-	7.941*ns	-	1.726×10^{-3}
(18^+)	2.922	45s	135.150s	99.93	100

Chapter 5

Formulation of Elastic Alpha Scattering

A nuclear reaction may take place when a projectile nucleus comes within a short range of a target nucleus. Within this range the interaction between the projectile and target nucleus is significant enough to cause the projectile to scatter from the target nucleus.The probability of a reaction to occur is directly linked to an effective range or an effective reaction cross sectional area. In an alpha elastic scattering experiment, one observes the collision between a beam of incident particles ($^4_2$He) and a target material. A detector is placed so as to cover a small solid angle $d\Omega$ with respect to the target. It records the alpha particles which are scattering in a direction (θ, ϕ) with respect to the incident beam direction (z).

An enhancement of the α elastic scattering differential cross sections as been experimentaly observed at backward scattering angles for a number of nuclei. This phenomenon is known as Anomalous Large Angle Scattering (ALAS). [29] The ALAS phenomenon can not be reproduced by the normal Saxon Woods optical model potential. Some phenomenological potentials like a molecular type, a squared Saxon Woods and SW + SW^3 were used to give a good account for the ALAS and produce satisfactory fits to the angular distributions for small range of nuclei [9, 10, 29]. We apply the mass symmetric SW + SW^3 optical model potential to light as well as heavy nuclei at different incident energies to reproduce the angular distributions of the α-elastic scattering differential cross sections up to back angles.

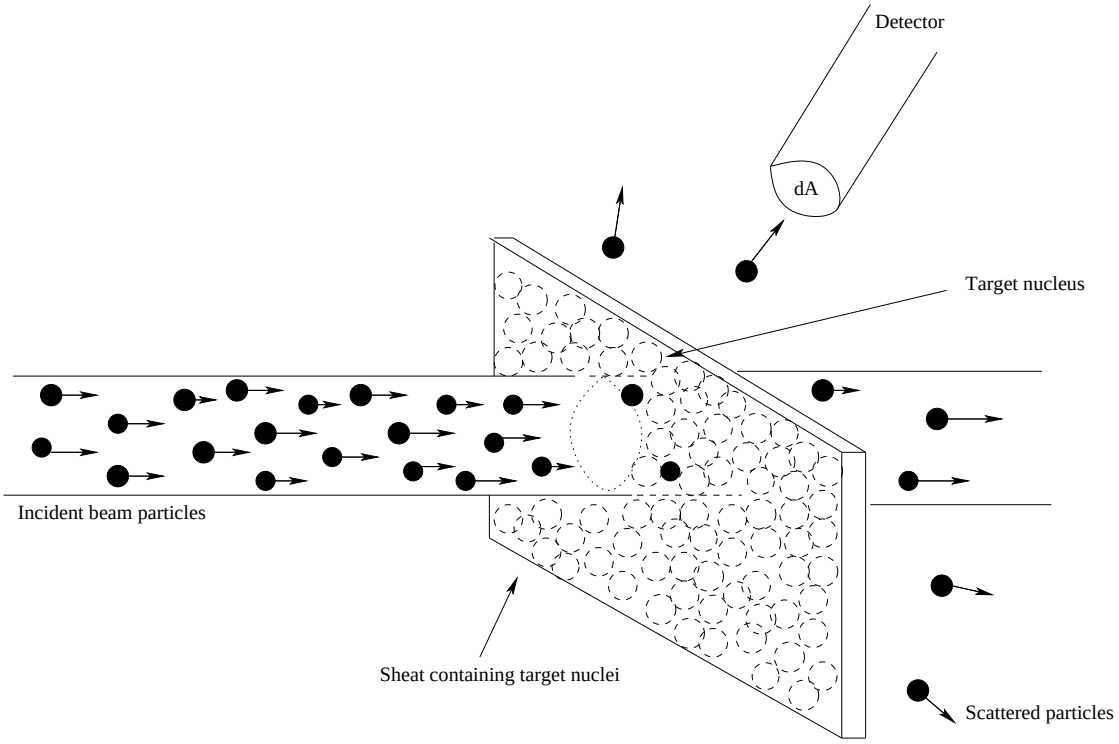

FIG. 5.1. Schematic of classical representation of the alpha elastic scattering.

5.1 Classical Representation of Differential Cross Section

A classical representation of differential cross-section can be explained in the following terms: I_a representing the current of incident particles, N_x the target nuclei per unit area and R_b the reaction rate. R_b is proportional to the product of I_a and N_x. We can write $R_b = \sigma I_a N_x$, $\sigma = R_b/I_a N_x$.

We call the proportionality constant σ the cross-section with the dimension of area/nucleus and σ can be larger or smaller than the geometric area of a nucleus. As the detector only covers a small solid angle $d\Omega$, it does not observe all the outgoing particles, only a fraction dR_b is observed. Generally the outgoing particles are not uniformly distributed, but will have an angular distribution depending on both θ and possibly ϕ. If we let $n(\theta, \phi)$ represent the angular distribution function for the outgoing particles, then $dR_b = n(\theta, \phi)\dfrac{d\Omega}{4\pi}$,

$$d\sigma = \frac{n(\theta, \phi)}{I_a N_x}\left(\frac{d\Omega}{4\pi}\right) \tag{5.1}$$

thus

$$\frac{d\sigma}{d\Omega} = \frac{n(\theta,\phi)}{4\pi I_a N_x}, \tag{5.2}$$

this is called the differential cross section [29].

5.2 Quantum Mechanical Representation of Differential Cross Section

Quantum mechanically, the differential cross section for elastic scattering between two spinless, non-relativistic particles with masses m_1 and m_2, is obtained by solving the Schrödinger equation describing the interaction of two particles through a potential $V(\vec{r}_1, \vec{r}_2)$ where $\vec{r}_1$ and $\vec{r}_2$ represent respectively the position of the two particles m_1 and m_2 from the origin, to give the elastic scattering cross section as function of the incident energy. The asymptotic form of the wavefunction is that of a plane wave representing the incident beam together with outgoing spherical waves of the same energy representing the elastically scattered particles. The structure of the scattered wave (angular dependence) depends on the potential $V(\vec{r}_1, \vec{r}_2)$.
For the time independent interaction and depending only on the relative distance r between the two interacting particles, the Schrödinger equation becomes

$$-\frac{\hbar^2}{2\mu}\nabla^2\psi(\vec{r}) + V(r)\psi(\vec{r}) = E\psi(\vec{r}). \tag{5.3}$$

At large distance away from the target centre, the potential becomes negligibly small so that

$$(\nabla^2 + k^2)\psi(\vec{r}) = 0, \tag{5.4}$$

where $k^2 = 2\mu E/\hbar^2$, with E the incident kinetic energy, μ the reduced mass as defined in Eq. (2.1) and $\hbar$ a Planck constant.
The solution corresponding to a plane wave incident in the $\vec{k}$ direction is

$$\varphi_{inc} = Ae^{i\vec{k}.\vec{r}}. \tag{5.5}$$

For a spherically symmetric scattered wave and at large distances away from the scattering region, the wave amplitude drops as $1/r$;

$$\varphi_{sc} \sim A\frac{e^{ik.r}}{r}. \tag{5.6}$$

as $\vec{k}$ and $\vec{r}$ are parallel to each other.

In general the scattered wave is not spherically symmetric, but depends on the direction of scattering (θ, ϕ), hence

$$\varphi_{sc} = Af(\theta, \phi)\frac{e^{ikr}}{r}, \tag{5.7}$$

where $f(\theta, \phi)$ is the scattering amplitude.

The total wave function is a superposition of the incident and scattered wave;

$$\psi(\vec{r}) = \varphi_{inc}(\vec{r}) + \varphi_{sc}(\vec{r}) = A\left[e^{i\vec{k}.\vec{r}} + f(\theta, \phi)\frac{e^{ik.r}}{r}\right]. \tag{5.8}$$

If there is azimuthal symmetry around the z-axis, the scattering amplitude $f(\theta, \phi)$ reduces to a function $f(\theta)$ of θ.

The probability for the incident particles to be scattered within the solid angle $d\Omega$ is related to the cross section $d\sigma(\theta)$ which is given by the ratio between the flux of the waves scattered through the surface subtended by the solid angle $d\Omega$, $d\Sigma = r^2 d\Omega$, and the flux of the incident plane waves through the unit surface. The scattered wave flux is given by

$$|J_{sc}|d\Sigma = \left|\frac{\hbar}{2i\mu}\left[f^*(\theta)\frac{e^{-ikr}}{r}\nabla f(\theta)\frac{e^{ikr}}{r} - f(\theta)\frac{e^{ikr}}{r}\nabla f^*(\theta)\frac{e^{-ikr}}{r}\right]\right| d\Sigma = v|f(\theta)|^2 d\Omega, \tag{5.9}$$

where the symbol J_{sc} represents the current density of the scattered wave flux. For elastic scattering, the incident wave flux is given by the two particle relative velocity $v = \hbar/\mu$ [29]. Thus the elastic scattering differential cross-section is

$$\frac{d\sigma(\theta)}{d\Omega} = |f(\theta)|^2. \tag{5.10}$$

Using the Born approximation and expanding the wavefunction in spherical waves, the scattering amplitude regarding to small phase shifts, can be written in integral form [29],

$$f(\theta) = -\frac{1}{K}\int_0^\infty \sin(Kr)U(r)r dr \tag{5.11}$$

where $U(r) = \dfrac{2\mu}{\hbar^2}V(r)$ and $K = 2k\sin(\theta/2)$, with $k^2 = \dfrac{2\mu}{\hbar^2}E$ and $k^2 \gg |U(r)|$.

Numerically this integral upper limit becomes

$$f(\theta) = -\frac{1}{K}\int_0^{\mathrm{D}} \sin(Kr)U(r)r dr \tag{5.12}$$

where D represents the impact parameter.

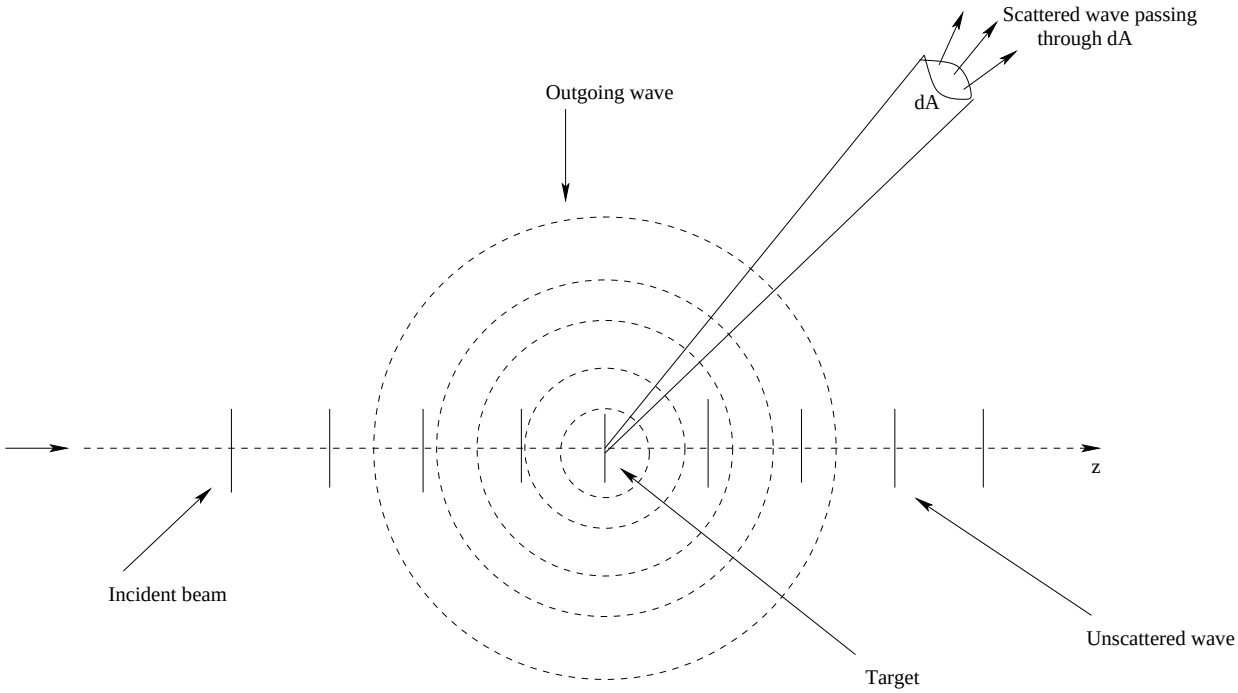

FIG. 5.2. Schematic of quantum representation of the elastic scattering.

For a real potential, only elastic scattering can take place and the phase angle of the wavefunction changes as a result of the action $V(r)$. In general, elastic as well as inelastic scattering can take place. Such a situation is represented by a complex scattering potential with the imaginary part representing the loss of probability from the incident channel due to such inelastic events as excitation of the target nucleus and projectile particle, absorption of the incident particles by the target and occurence of nuclear reactions. In such cases, the phase shifts are complex [30]. Hence the scattering potential has a complex form $V(r) = U(r) + iW(r)$

5.3 Optical Model

In a nuclear reaction process, at a given bombarding energy (E), the nucleus behaves like a light scattering cloudy crystal ball and hence the name optical model. The aim of the optical model is to find a potential to describe variations of the scattering cross section as a function of the incident kinetic energy E and target nucleon number A. Some semi-

empirical forms of the optical potential have been used over the years with great success for (< 200 MeV) scattering. These potentials may be of the Saxon Woods form and its modifications like Michel potential and molecular potential [30]. The Squared Saxon-Woods Michel potential and the molecular potential provide successful description of α-elastic scattering for quite a number of light nuclei at a significant range of incident energies [29]. However, the values of the Coulomb radii for the molecular potential are suspicious, they are an order of 3 magnitudes too large. Also, the ambiguities in the choice of the real and imaginary parts of the Michel potential, and the considerable deep difference between the Michel and molecular potentials, require further investigations.

Different theoretical approaches were used to describe the experimental elastic data for α-scattering by ^{16}O [31, 32], ^{90}Zr [33-35] and ^{40}Ca [36-41]. However none of them could simultaneously describe the significant back angle α-scattering for these three nuclei. There is still a need for an optical model potential which can fit to the observable cross section in the ALAS region in general [42].
In the next chapter we investigate the optical potentials which theoretically describe ALAS.

Chapter 6

Theoretical Predictions of α-Elastic Scattering Observables

6.1 Real Optical Potential

The mass symmetric Saxon-Woods plus cubed Saxon-Woods potential which gives a good account to the spectra and the α-decay properties, is tested for description of the elastic α-scattering. This phenomenological potential form (mass symmetric SW + SW^3) as given in Eq. (4.1) is used as the real optical potential by maintaining the radius R of each nucleus and other parameters of the real part ($U_o = 54$ MeV, $a = 0.73$ fm and $x = 0.35$).

The maximum L-value of partial waves is internally selected in the code and typically $L - max = 7\mathrm{k} + \mathrm{k}R \leqslant 99$, where k the wave number and R the nuclear radius. The impact parameter is equal to 7.5 fm + R.
We then fit the experimental elastic α-scattering differential cross section data of each nucleus by a suitable imaginary optical potential form with only one free parameter.

6.2 The Imaginary Optical Potential

The imaginary part is adjusted freely and parametrized by a Squared Saxon-Woods function

$$W(r) = \frac{W_o}{\{1 + \exp\left[(r - R_W)/2a_W\right]\}^2} \tag{6.1}$$

for the α+^{40}Ca, α+^{90}Zr and α+^{208}Pb systems and the surface peaked Saxon-Woods derivative form

$$W(r) = \frac{-4W_o \exp[(r - R_W)/a_W]}{\{1 + \exp[(r - R_W)/a_W]\}^2} \tag{6.2}$$

for the α+^{16}O system [43].
The choice of imaginary potential forms is arbitrary given that the fit is insensitive to the precise form of imaginary part of the potential.

6.3 Fitting of Imaginary Potential Depth

To fit the measured angular elastic distributions, the imaginary potential diffuseness is fixed at $a_W = 1.0$ fm, the imaginary potential radius R_W is constrained to be equal to the radius parameter R of the real potential, and the imaginary potential depth W_o is adjusted separately at each energy to reproduce the data as well as possible. For suitable imaginary potential depth value, the following quantity L, must be minimized as,

$$L = \sum_i \left[\frac{\left(\frac{d\sigma}{d\Omega}\right)_i^{exp} - \left(\frac{d\sigma}{d\Omega}\right)_i^{theor}}{\Delta\left(\frac{d\sigma}{d\Omega}\right)_i^{exp}} \right]^2 \tag{6.3}$$

where $(d\sigma/d\Omega)_i^{expt}$ is the observed value , $(d\sigma/d\Omega)_i^{theor}$ the predicted value and $\Delta(d\sigma/d\Omega)^{expt}$ the experimental error at the i^{th} measured angle respectively [43].
The suitable values of W_o are given in Tables (6.1 and 6.2).

TABLE. 6.1. Imaginary potential depths for α+^{16}O and α+^{40}Ca systems. Best fit values of the imaginary potential depths W_o (MeV) obtained at different incident energies E (MeV).

α+^{16}O		α+^{40}Ca	
E (MeV)	W_o (MeV)	E (MeV)	W_o (MeV)
22.0	0.98	24.1	31.33
25.4	5.69	29.0	34.74
26.6	5.71	39.6	47.45
30.0	5.69	49.5	49.75
39.3	7.15		
49.5	10.07		

TABLE. 6.2. Imaginary potential depths for α+^{90}Zr and α+^{208}Pb systems. Best fit values of the imaginary potential depths W_o (MeV) obtained at different incident energies E (MeV).

α+^{90}Zr		α+^{208}Pb	
E (MeV)	W_o (MeV)	E (MeV)	W_o (MeV)
21.0	27.18	23.4	106.21
23.4	29.97	40.0	18.49
25.0	38.73	58.0	126.49
40.0	40.35		

6.4 Elastic Differential Cross Sections

We remark that the theoretical elastic differential cross sections of ^{16}O$(\alpha,\alpha)^{16}$O are very good at the small angles as well as at the ALAS region, but are poorly reproduced at the angles between 50° and 115°. At 22.0 MeV and 39.3 MeV incident energies, the theoretical curves are below the experimental structure at the angles from 42° to 62° while they are above it at the angles from 63° to 115°. At 26.6 MeV incident energy, the theoretical curve is slightly out of phase from 54° to 84° and a similar shape is remarked at 25.4 MeV and 26.6 MeV incident energies from 38° to 84°. At 49.5 MeV, the trend of theoretical predictions is generally good.

In the case of ^{40}Ca$(\alpha,\alpha)^{40}$Ca (see Fig. 6.2), apart the difference between the two curves at 29.0 MeV from 60° to 84° MeV and at 39.6 MeV from 65° to 85° where the theoretical curves are below the experimental ones, the trend of the theoretical predictions is in good

agreement with the experiment.

For ^{90}Zr$(\alpha,\alpha)^{90}$Zr (see Fig. 6.3), only the elastic differential cross sections are satisfactorily reproduced at 40 MeV incident energy, the description at 25 MeV, 23.4 MeV and 21 MeV incident energies is poor. The theoretical predictions at these three incident energies are well reproduced at the angles between 42° and 80°, but beyond that the theoretical curves are much below the experimental data.
The theoretical predictions of ^{208}Pb$(\alpha,\alpha)^{208}$Pb shown in Fig. 6.4 nicely reproduced the experimental data. A small deviation is only observed at 58.0 MeV from 69° to 88°. We extrapolate the theoretical calculations to large angles where the measured values are not yet available.
The mass symmetric SW + SW^3 potential generally gives a satisfactory description of the alpha elastic scattering for α+^{16}O, α+^{40}Ca and α+^{208}Pb, especially the ALAS is very well reproduced. Only the description for α+^{90}Zr is poorly reproduced. The results for the elastic differential cross-sections are displayed in Figures (6.1 - 6.4), where the solid lines represent the theoretical values and the circles correspond to the experimental data.

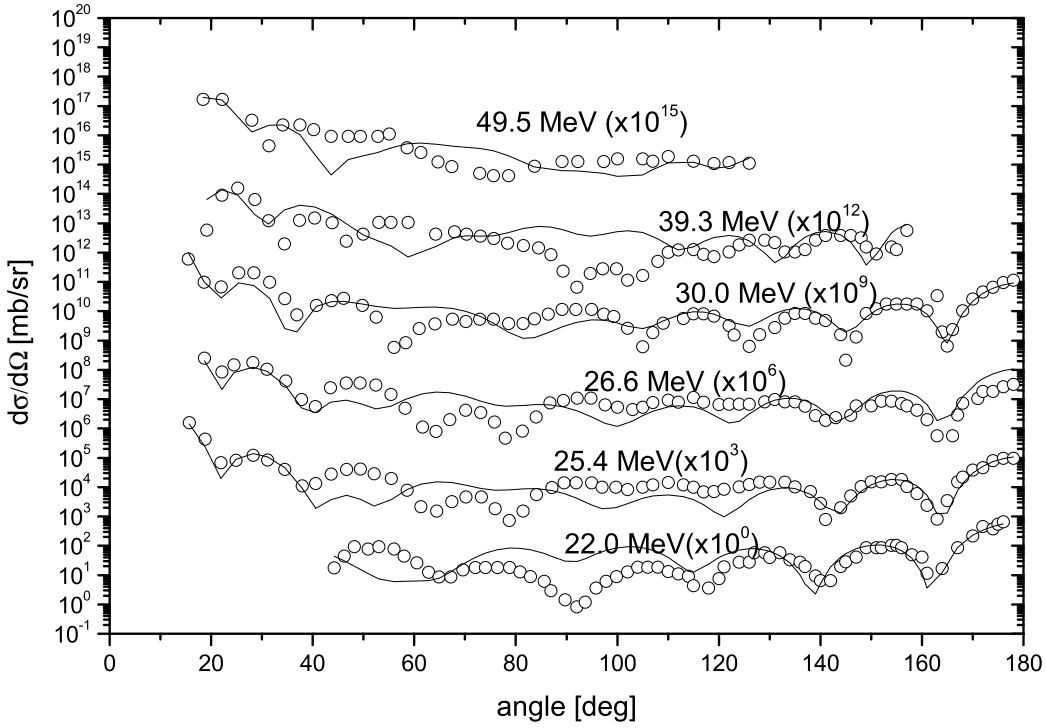

FIG. 6.1. Elastic differential cross sections at various incident energies for $^{16}\mathrm{O}(\alpha,\alpha)^{16}\mathrm{O}$. Comparison of the differential cross section predictions of the global potential of Eq. (4.1. and 6.2.) with the experimental data. The corresponding imaginary potential depth values are given in Table 6.1. The experimental data are taken from [43].

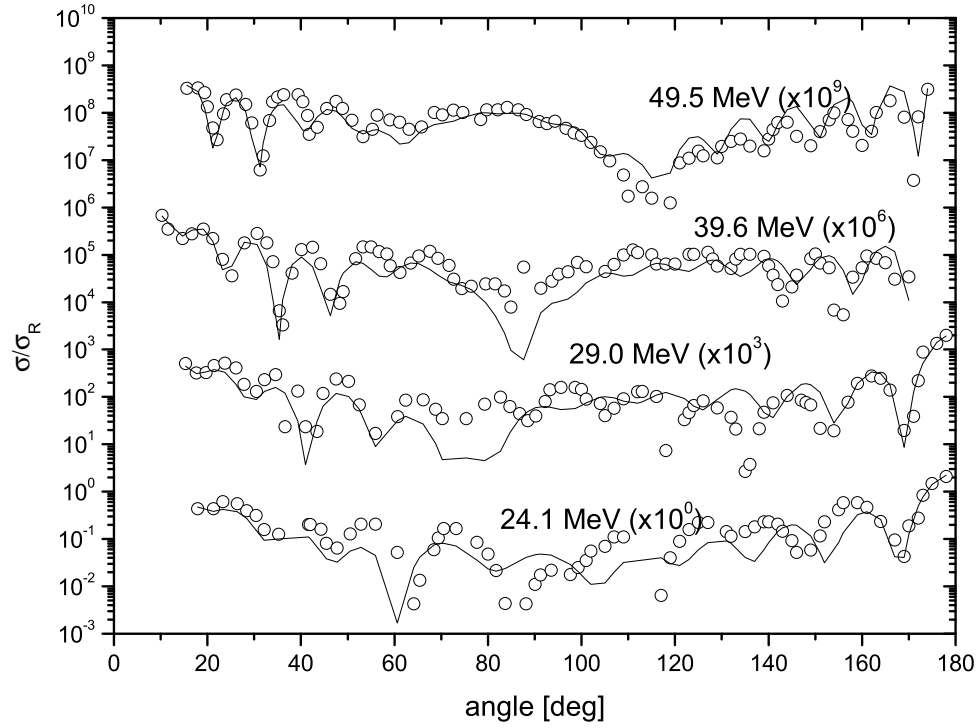

FIG. 6.2. Elastic differential cross sections at various incident energies for ^{40}Ca$(\alpha,\alpha)^{40}$Ca. Comparison of the differential cross section predictions of the global potential of Eq. (4.1. and 6.1.) with the experimental data. The corresponding imaginary potential depth values are given in Table 6.1. The experimental data are taken from [43].

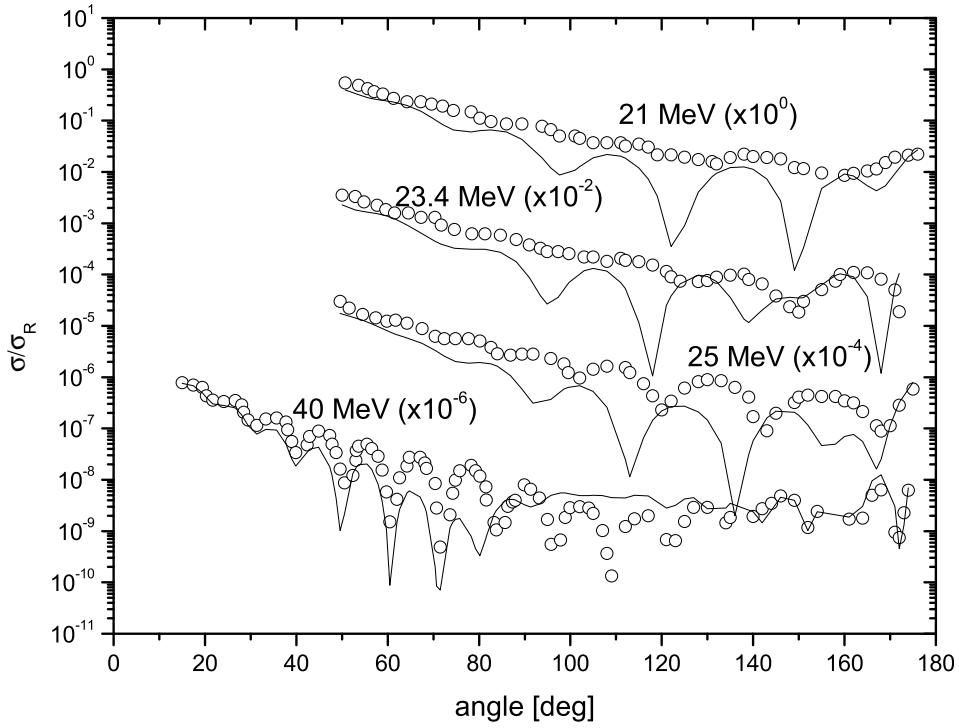

FIG. 6.3. Elastic differential cross sections at various incident energies for ^{90}Zr$(\alpha,\alpha)^{90}$Zr. Comparison of the differential cross section predictions of the global potential of Eq. (4.1. and 6.1.) with the experimental data. The corresponding imaginary potential depth values are given in Table 6.2. The experimental data are taken from [35].

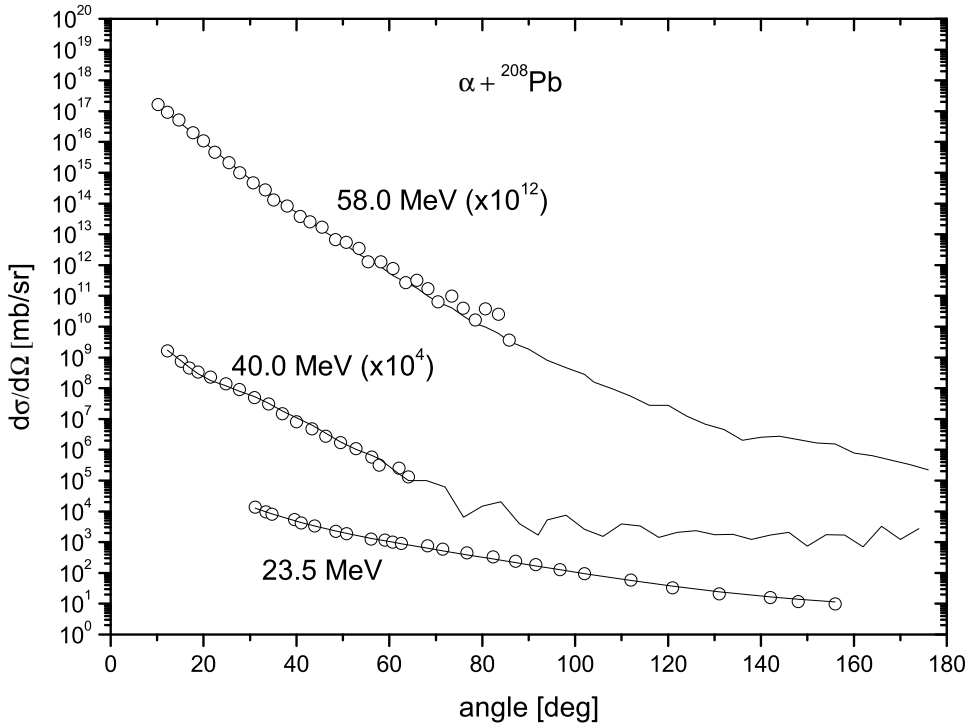

FIG. 6.4. Elastic differential cross sections at various incident energies for ^{208}Pb$(\alpha,\alpha)^{208}$Pb. Comparison of the differential cross section predictions of the global potential of Eq. (4.1. and 6.1.) with the experimental data. We extrapolate the predictions to large angles where the experimental data are not yet available. The corresponding imaginary potential depth values are given in Table 6.2. The experimental data are taken from [8].

Chapter 7

Conclusion

We have used the mass symmetric SW + SW^3 phenomenological potential model to study the structure of five nuclei (^{20}Ne, ^{44}Ti, ^{94}Mo, ^{136}Te and ^{212}Po) which have been modeled in terms of a doubly closed shell core plus an α cluster formed by the strongly correlated motion of the valence nucleons.

Using the potential parameters (U_o = 54 MeV, a = 0.73 fm) as obtained by Buck *et al.* [52] and refining the effect of the SW^3 term at $x = 0.35$, we have optimised the radius of each nucleus to simultaneously describe the low-lying positive parity states and the quadrupole transition strengths $B(E2 : L_i \rightarrow L_f)$ for the ground state band of the five nuclei, as well as the α decay half-lives and α branching ratios of ^{212}Po.

The same potential has been used as the real part of an optical model, with a suitably chosen imaginary potential (containing only one adjustable parameter), to describe the α elastic scattering from ^{16}O, ^{40}Ca, ^{90}Zr and ^{208}Pb.

The results for the energy spectra, electromagnetic transition rates, α decay half-lives and α branching ratios are in good agreement with experiment. The suggested potential form also gives a reasonable account of the differential cross-sections of alpha elastic scattering from ^{16}O, ^{40}Ca and ^{208}Pb, and in particular of the ALAS for α+^{16}O and α+^{40}Ca. We have extrapolated the theoretical predictions of α+^{208}Pb to large angles where the experimental data are not yet available.

However, this potential fails to describe well the alpha elastic scattering from ^{90}Zr at different incident energies. Some work is still needed to improve the model in this case, possibly by fine tuning the parameter values.

In view of a successful description of the α structure properties of five nuclei and the theoretical differential cross sections of three systems (α+^{16}O, α+^{40}Ca and α+^{208}Pb) using a single real potential shape with the real potential radius and imaginary potential depth as the only changing parameters from one nucleus to the other, we argue that alpha clustering must be an essential ingredient for quantitatively understanding the properties of these doubly closed shell + alpha nuclei and strongly suggest the existence of a universal potential.

Appendix A

Analysis for ^{8}Be

We extend the application of the potential given in Eq.(4.1) to the very light nucleus ^{8}Be modelled as an alpha core + an alpha cluster. We find the radius $R = 1.67755$ fm (1.057 $A^{1/3}$) with G = 4, which reproduces the known Q-value $Q_o = 0.093$ MeV of the ^{8}Be ground state. The 2^+ state of ^{8}Be is then found to be unbound.
We then calculate the alpha decay half-life of the ground state. The theoretical alpha decay is in good agreement with the experiment. We find the calculated value $\Gamma_{\text{theor.}} = 12.5$ eV compared to the experimental value $\Gamma_{\text{exp.}} = 5.57$ eV. The corresponding theoretical half-life is given by $T_{1/2} = \dfrac{\hbar \ln 2}{\Gamma_{\text{theor.}}} = 3.664 \times 10^{-17}$ s.

Fig.A.1. shows a comparison between the alpha - alpha nuclear potential of Eq. (4.1.), and the local Gaussian potential

$$V(r) = -V_0 \exp(-\alpha r^2), \tag{A.1}$$

with parameter values $V_0 = 122.6225 MeV$ and $\alpha = 0.22$ fm^{-2}, which gave a good account of the alpha - alpha elastic scattering phase shifts up to 40 MeV incident centre of mass energy. We conclude that our potential will result in good fits to the alpha - alpha scattering data [43].

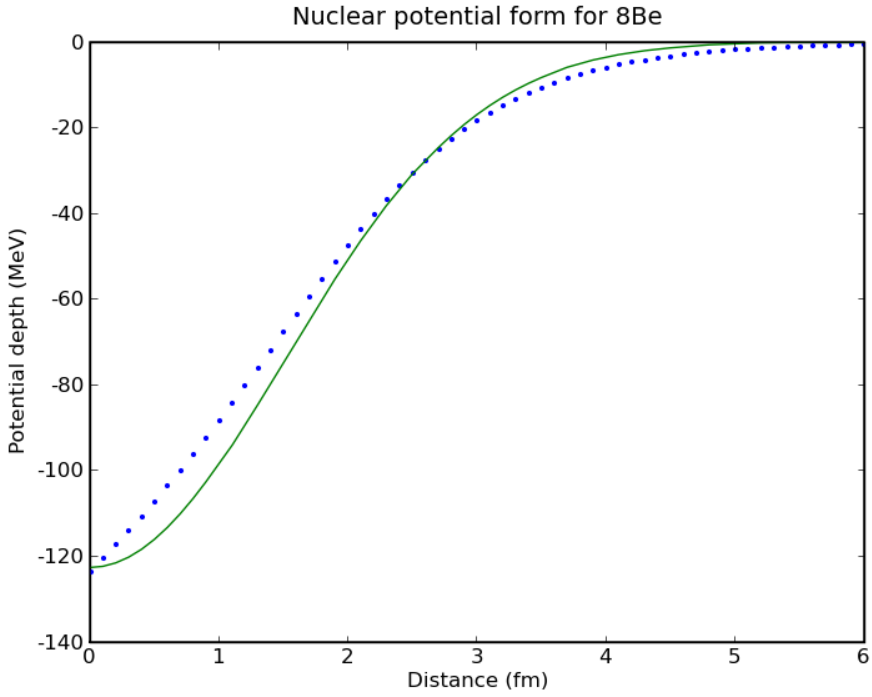

FIG. A.1. A comparison of the mass symmetric SW + SW^3 nuclear potential from Eq. (4.1) (dot line) for ^{8}Be with the radius R= 1.67755 fm and the local Gaussian potential from Eq. (A.1) (solid line), which gave a good account of the $\alpha - \alpha$ elastic scattering phase shifts.

When we artificially shift down the states by changing the Q-value $Q_0 = 0.093$ MeV to $Q_0' = -0.907$ MeV and fit the radius to R= 1.821 fm (1.147 $A^{1/3}$), we can estimate the actual gap between the 0^+ and 2^+ states. This yields E_2^* theor. = 2.874 MeV in good agreement with E_2^* exp. $= 3.03 \pm 0.01$ MeV.

Appendix B

Fitting Nuclear Structure Properties

We have used programmes for the calculations described in this thesis. The decay half-life and fitting spectra involve integrals whose limits are the classical turning points r_1, r_2 and r_3 which were determined using a combination of the incremental search and bisection methods to obtain the roots of a function

$$f(r) = Q + E_L^* - V(r, R) \tag{B.1}$$

where Q is the Q-value of the exotic decay of the nucleus (in its ground state) into the core and cluster, and E_L^* is the excitation energy of the L^{th} member of the ground state band.

Based on the fact that a root either falls in a given interval (a,b) or equal to one of the boundary values a,b if $f(a)f(b) \leqslant 0$, and depending on the size of a nucleus, we define the initial region containing the turning points and determine the smallest interval containing the root of the function by using the incremental search method. The exact root within the smallest interval is then obtained with the bisection method to an accuracy of 10^{-5}.

The integrals were calculated by employing the extended method

$$\int_a^b f(r)dr = h\left[f(a + h/2) + f(a + 3h/2) + f(a + 5h/2) + ... + f(b + h/2)\right] \tag{B.2}$$

where h is the step size of the order 10^{-3}.

We then use the Bohr-Sommerfeld (BS) quantization integral to calculate the alpha decay half-lives and optimise the radius to reproduce well the experimental energy levels.

Appendix C

Fitting Elastic α-Scattering

We have used a standard code SNOOPY8 [44] to fit the elastic α-scattering. The program performs calculations of the elastic scattering differential cross sections of particles of spin s=0, 1/2 or 1 from a nucleus whose spin is ignored. SNOOPY8 can perform calculations with up to 100 experimental input data (differential cross-sections values and corresponding angles).

Automatic searches for potential parameters (up to 8 possible) giving best fits to cross sections can simultaneously be made, in such a way that the chi-squared deviation between experimental and calculated quantitatives is minimised. However more than 4 to 6 parameters usually are impractical because of parameter correlations. Successive searches with different parameter combinations are recommended. The iteration process is terminated either when externally specified convergence criteria have been met or when built-in limits are reached. The minimum percentage change in chi-squared between successive iterations which terminates search is 0.1 by default. A zero initial value for a parameter to be varied is not permitted and may cause abnormal job termination.

Appendix D

Plots for Comparison Between The Experimental and Calculated Energy Levels.

With use of the nuclear potential given in Eq. 4.1, we find that the level sequence and the compression of the higher spin states of ^{212}Po are well reproduced with the 16^+ state above the 18^+ state which provides an explanation for the isomeric nature of the 18^+ state . The calculated spectra for the nuclei investigated are generally in good agreement with experiment, as shown in Fig. D.1 to D.3.

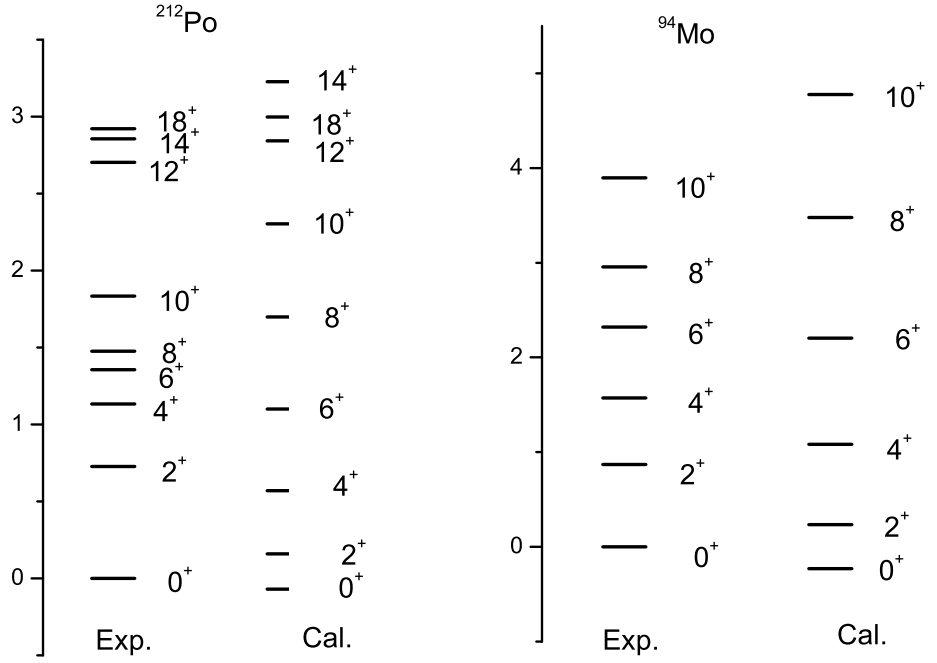

FIG. D.1. Excitation energies of the low-lying positive parity states in ^{212}Po and ^{94}Mo. Experimental values Expt. E* (MeV) are compared with their calculated counterparts Calc. E* (MeV) obtained using the SW + SW^3 potential of Eq. (4.1) with $U_0 = 54$ MeV, $a = 0.73$ fm, and $x = 0.35$.

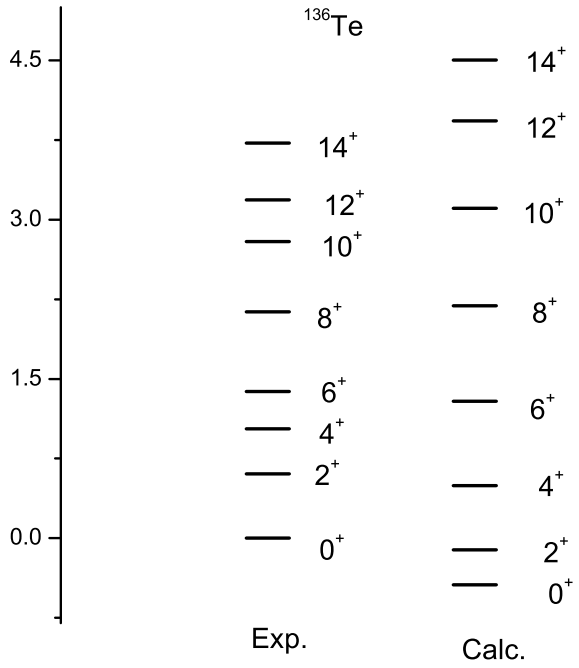

FIG. D.2. Excitation energies of the low-lying positive parity states in ^{136}Te. Experimental values Expt. E* (MeV) are compared with their calculated counterparts Calc. E* (MeV) obtained using the SW + SW^3 potential of Eq. (4.1) with $U_0 = 54$ MeV, $a = 0.73$ fm, and $x = 0.35$.

.

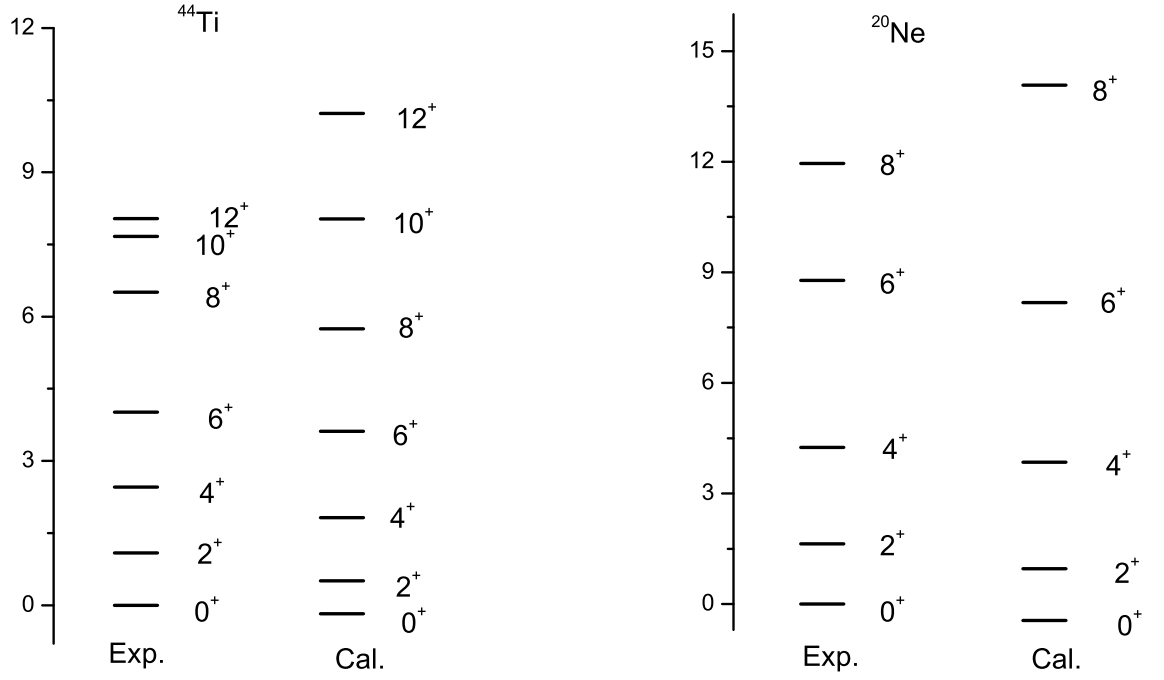

FIG. D.3. Excitation energies of the low-lying positive parity states in ^{44}Ti and ^{20}Ne. Experimental values Expt. E* (MeV) are compared with their calculated counterparts Calc. E* (MeV) obtained using the SW + SW^3 potential of Eq. (4.1) with $U_0 = 54$ MeV, $a = 0.73$ fm, and $x = 0.35$.

Bibliography

[1] E. N. Da and C. Andrade, *Rutherford and the Nature of the Atom* (Heinemann, London, 1965).

[2] K. Krane, *Introductory Nuclear Physics* (Sons, New York, 1988).

[3] C. Batty and G. Greenless., Nucl. Phys. A **133**, 673 (1969).

[4] A. Bohr and B. Mottelson, *Nuclear Structure Volume 2: Nuclear Deformations* (World Scientific, London, 1975).

[5] K. Ikeda, Proc. Fifth Int. Conf. Clustering Aspects in Nucl. and Sub-nucl Systems, Kyoto 1988. J. Phys. Soc. Jpn. **58**, 277 (1989).

[6] B. Buck, A. C. Merchant, and S. M. Perez, Phys. Rev. Lett. **65**, 2975 (1990).

[7] B. Buck, A. C. Merchant, and S. M. Perez, J. Phys. G. **17**, 1223 (1991).

[8] B. Buck, A. C. Merchant, and S. M. Perez, Phys. Rev. C. **45**, 2247 (1992).

[9] B. Buck, J. Johnson, A. C. Merchant, and S. M. Perez, Phys. Rev. C. **53**, 2841 (1995).

[10] B. Buck, A. C. Merchant, and S. M. Perez, Phys. Rev. C. **51**, 559 (1994).

[11] B. Buck, A. C. Merchant, and S. M. Perez, Nucl. Phys. A. **652**, 211 (1999).

[12] B. Buck, A. C. Merchant, and S. M. Perez, Nucl. Phys. A. **657**, 267 (1999).

[13] B. Buck, A. C. Merchant, and S. M. Perez, Phys. Rev. C. **71**, 014311 (2005).

[14] B. Buck, A. C. Merchant, and S. M. Perez, Nucl. Phys. A. **673**, 157 (2000).

[15] S. DeBenedetti., *Nuclear Interactions* (John Wiley and Sons, Inc., New York . London . Sydney, 1964).

[16] N.Zettili, *Quantum Mechanics: Concepts and Applications* (John Wiley and Sons, 2001).

[17] K.Gettfried and T. Yan, *Quantum Mechanics: Fundamentals* (Springer, New York, 2004).

[18] T. Ibrahim, *PhD Thesis* (Stellenbosch University, 2009).

[19] H. Seal, *MSc Thesis* (University Of Cape Town, 2006).

[20] J. Blatt and V. Weisskopf, *Theoretical Nuclear Physics* (John Willey and Sons, New York, 1952).

[21] B. Buck, A. C. Marchant, M. J. Horner, and S. M. Perez, Phys. Rev. C **61**, 024314 (2000).

[22] B. Buck, A. C. Merchant, and S. M. Perez, Nucl. Phys. A. **614**, 129 (1997).

[23] D. M. Brink and G. R. Satchler, *Angular Momentum* (Oxford Univ. Press, N.Y, 1993).

[24] P. T. Matthews, *Introduction to Quantum Mechanics* (Mc Graw-Hill, London, 1968).

[25] S. A. Gurvitz and G. Kälbermann, Phys. Rev. Lett. **59**, 1987 (1987).

[26] I. Perlman and J. O. Rasmussen, Handb. Phys. XLII **109** (1957).

[27] B. Buck, A. C. Merchant, and S. M. Perez, Phys. Rev. C. **47**, 1307 (1993).

[28] A. Astier *et al.*, arXiv. **1004.1517 V1 [nucl-ex],** (9 Apr. 2010).

[29] A. S. Tarik and A. F. M. Rahman, Phys. Rev. C **59**, 2558 (1998).

[30] C. Cohen and B. Diu., *Quantum Mechanics* (Herman, John Wiley and Sons, 1977).

[31] F. Michel *et al.*, Phys. Rev. C **28**, 1904 (1983).

[32] F. Michel, G. Reidemeister, and Y. Kondo, Phys. Rev. C **51**, 3290 (1995).

[33] F. Michel, A. Reidemeister, and Y. Kondo, Phys. Rev. C. **61**, 041601(R) (2000).

[34] Shigeo, Phys. Rev. Lett. **74**, 2176 (1994).

[35] M. Wit, J. Schiele, K. A. Eberhard, and J. P. Schiffer, Phys. Rev. C **12**, 1447 (1975).

[36] A. C. Merchant, Phys. Rev. C **36**, 778 (1987).

[37] F. Michel, G. Reidemeister, and S. Ohkubo, Phys. Rev. C **37**, 292 (1987).

[38] S. Ohkubo, Phys. Rev. C **38**, 2377 (1987).

[39] G. Reidemeister, S. Ohkubo, and F. Michel, Phys. Rev. C **41**, 63 (1989).

[40] T. Derbar *et al.*, Phys. Rev. C **18**, 1237 (1978).

[41] F. Michel, G. Reidemeister, and Ohkubo, Phys. Rev. Lett. **57**, 1215 (1986).

[42] N. S. Wall, Phys. Rev. C. **14**, 2326 (196).

[43] B. Buck, A. C. Merchant, and S. M. Perez, Phys. Rev. C. **52**, 1840 (1995).

[44] P. Schwandt, *SNOOPY8-Version 6/01/82* (Indiana University, Bloomington, 1982).